Journal of Alloys and Compounds 1003 (2024) 175683

Contents lists available at ScienceDirect

Journal of Alloys and Compounds

journal homepage: www.elsevier.com/locate/jalcom

Review

# Mechanistic investigations of emerging type-II, Z-scheme and S-scheme heterojunctions for photocatalytic applications – A review

Alisha Shabbir [a], Sabahat Sardar [b], Asad Mumtaz [a,*]

[a] Department of Chemistry, School of Natural Sciences (SNS), National University of Sciences and Technology (NUST), H-12, Islamabad 44000, Pakistan
[b] Research and Development (R&D) Division, Al Qasim Traders, H-13, Islamabad 44000, Pakistan

ARTICLE INFO

*Keywords:*
Photocatalysis
Photocatalytic water splitting
Photodegradation
$CO_2$photoreduction
$H_2O_2$ production
Photoelectrochemical water splitting
Dye degradation using semiconductors
Hetrostructures
Heterojunctions
Solid-state Z-scheme heterojunctions

ABSTRACT

Photocatalysis is considered to be the most promising route for remediation of the environment by degradation of pollutants and production of environment friendly fuels. There are two major factors that affect the efficiency of photocatalysts that are (i) poor light absorption in visible regions and (ii) photoexcited charge separation and transportation in heterojunctions. These problems are solved by formation of heterojunctions between two or more semiconductors which enhance their photocatalytic activities. Effective charge transfer at the heterojunction is a key factor required to explore further as the already developed schemes have the major technicalities to address for the enhanced photoexcited charge production and separation via effective interface, without losing effective electrons required for boosting the rates of various reactions at the surface sites of the photocatalysts. This review gives an overview of photocatalytic activities, and construction of various types of heterojunctions between metal oxide-metal oxide, metal oxide-metal sulfide and metal sulfide-metal sulfide-based heterostructures. The band gap adjustments and alignments in various types of emerging heterojunctions are explored and correlated to establish structure-photoactivity relationship and photostability of metal oxides and metal sulfides with established binary, ternary and quaternary composites. This study has paved the potential ways to design efficient heterojunction-based strategies for photocatalytic applications.

## 1. Introduction

The accessibility of renewable energy sources, clean water and environment are considered to be major challenges in recent years. The development of the industries and human society is strongly depended on fossil fuels which causes excessive emission of greenhouse gases and increases environmental pollution. Therefore, there is a need of development of environmentally friendly energy resources such as semiconductor-photocatalysis [1]. Thus, Photocatalysis is the process in which visible light having energy equal to or greater than its band gap energy is adsorbed on the surface of semiconductor catalyst (SC) which causes excitation and migration of electrons and holes to its conduction band and valence band. The reaction involves in this process is [2]:

$$\mathbf{SC + h\nu \rightarrow h^{+}\, e^{-}}$$

$\mathbf{h^{+}\, e^{-}} \rightarrow h^{+}_{VB} + e^{-}_{CB}$ To obtain pollution free environment there are some treatments required such as; water splitting, dye degradation,$CO_2$ reduction and $H_2O_2$ production (Fig. 1). Firstly, Photocatalytic water splitting is regarded as artificial photosynthesis because it is similar to the natural photosynthesis uses solar light by the green plants [3]. In this process, solar energy is converted into chemical energy while water splitting process promotes Gibbs free energy [4]. Generally, photocatalytic water splitting requires solar light, photoreactor, reactant (water) and photocatalyst to produce hydrogen [5]. The mechanism for photocatalytic water splitting for hydrogen production has four main processes which are (i) light harvesting (ii) charge excitation (iii) charge separation and transportation (iv) surface catalytic reactions [6]. This process starts with visible light irradiation having energy equal to or greater than band gap of the photocatalyst. The photocatalyst absorbs appropriate light energy and causes electronic transition and generates electron-hole pairs. The charges are separated and electrons are transferred from valence band to conduction band leaving the holes behind. The electrons and holes cause reduction and oxidation reaction with water and produce hydrogen and oxygen [7,8]. Contrarily, water splitting is an endothermic process [9] and requires source of energy to fulfill Gibbs free energy ($\Delta H^{\circ}$=238kjmol$^{-1}$ to rearrange the valence electrons for formation of $H_2$ and $O_2$ [10]. In order to produce one molecule of

---

* Corresponding author.
*E-mail address:* asad_032@yahoo.com (A. Mumtaz).

https://doi.org/10.1016/j.jallcom.2024.175683
Received 4 May 2024; Received in revised form 19 July 2024; Accepted 22 July 2024

hydrogen from water 2.458 eV energy is required. Since, two molecules of hydrogen are produced from water using four electrons and the energy will be required about 4.915 eV. These photons can be utilized by visible light with wavelength 504.5 nm to produce hydrogen [11,12]. When semiconductor uses sunlight higher than band gap energy then e-/h+ pairs are delocalized within semiconductor and causes electrons to attain internal equilibrium within energy level instead of across the band gap and these states are referred as Fermi levels. Under visible light illumination, electrons and holes are not generated by heat as the solar light is utilized as Gibbs free energy for photocatalytic water splitting [13,14]. The photocatalytic water splitting is represented in the following equations below:

$$2H^{+} \quad + \quad 2e^{-} \quad \rightarrow \quad H_2 E^{\circ}_{reduction} = 0.00 V_{NHE}$$

$$H_2O \quad + \quad 2h^{+} \quad \rightarrow \quad 2H^{+} \quad + \quad ½O_2 E^{\circ}_{oxidation} = 1.23 V_{NHE}$$

Secondly, photodegradation is broken down of larger species into low molecular weight, non-toxic and smaller species chemically under solar light illumination. The mechanism involves absorption of photon energy which is greater than or equal to band gap energy of the photocatalyst. The excitation of electrons occurs from the valence band to the conduction band which leads to formation of electrons and hole pairs. The photoexcited holes and electrons interact with dye molecules and produces dye*. These unstable dyes convert to dye$^{-}$ and dye$^{+}$ radicals. These positive and negative radicals spontaneously decompose to the degradation products [15]. The photodegradation of organic dyes is usually based on highly reactive OH radicals. These OH radicals are produced by the reaction of electrons and holes and the rate of reaction is expressed by Langmuir-Hinshelwood and Eley-Rideal mechanism $1/[P]_t = k_2 t + 1/[P]_0$ [16,17]. Thirdly, Photocatalytic $CO_2$ reduction mimics the natural photosynthesis in which solar light energy is used to convert $CO_2$ into more reduced species such as; CO, HCOOH, HCHO, $CH_3OH$, $CH_4$ and $C_2H_5OH$ [18,19]. Thermodynamics of $CO_2$ reduction involves redox reaction and positive Gibbs free energy values which is not favorable under standard conditions and requires energetically uphill [20,21]. It is non spontaneous process and requires an input of energy to proceed and is favorable at specific temperature and pressure conditions [22]. Therefore, the Gibbs free energy for $CO_2$ reduction to CO is 257kj/mol, HCOOH is 286kj/mol, HCHO is 522kj/mol, $CH_3OH$ is 703kj/mol and $C_2H_5OH$ is 818kj/mol [23]. Electrons are involved in the photoreduction of $CO_2$ and band gap plays an important role. It takes place if the conduction band level is higher than reduction potential of $CO_2$ and valence band is more positive than oxidation potential [24]. The photoreduction of $CO_2$ involves following equations:

$$\mathbf{CO_2 \quad + \quad e^{-} \rightarrow \quad CO_2^{-}} \quad E^{\circ}_{redox} = -1.9V$$

$$\mathbf{CO_2 + H^{+} + 2e^{-} \rightarrow HCOO^{-}} \qquad E^{\circ}_{redox} = -0.49V$$

$$\mathbf{CO_2 + 2e^{-} + 2H^{+} \rightarrow CO} \qquad E^{\circ}_{redox} = -0.53V$$

$$\mathbf{CO_2 + 4e^{-} + 4H^{+} \rightarrow HCHO} \qquad E^{\circ}_{redox} = -0.48V$$

$$\mathbf{CO_2 + 6e^{-} + 6H^{+} \rightarrow CH_3OH} \qquad E^{\circ}_{redox} = -0.38V$$

$$\mathbf{CO_2 + 4e^{-} + 8H^{+} \rightarrow CH_4} \qquad E^{\circ}_{redox} = -0.24V$$

Lastly, photocatalytic production of $H_2O_2$ is also governed by basic photocatalytic reaction principle. It can be generated through either a sequential two step single electron indirect process or one step two electron direct process route [25]. The indirect reduction process of photocatalytic $H_2O_2$ production involves production of superoxide radicals from one electron reduction of $O_2$ which further react with $H^{+}$ and form $OH_2^{\cdot -}$ radicals. This $OH_2^{\cdot -}$ undergoes one electron reduction and produce $OH_2^{-}$. This $OH_2^{-}$ finally reacts with $H^{+}$ and produce $H_2O_2$ product. Meanwhile, in the direct reduction process $O_2$ would directly reacts with two $H^{+}$ ions and produce $H_2O_2$ product using two electrons for photoreduction. This process is uphill reaction with standard Gibbs free energy change is 117kj/mol [26,27]. The reaction involves following equations:

$$2H_2O + 4H^{+} \rightarrow O_2 + 4H^{+}$$

$$O_2 + e^{-} \rightarrow O_2^{\cdot -}$$

$$O_2 + H^{+} \rightarrow HO_2^{\cdot -}$$

$$HO_2^{\cdot -} + e^{-} \rightarrow HO_2^{-}$$

$$HO_2^{-} + H^{+} \rightarrow H_2O_2$$

$$O_2 + 2H^{+} + 2e^{-} \rightarrow H_2O_2 \qquad E^{\circ}_{redox} = 0.68V$$

Similarly, computational simulations were also applied to study the semiconductor-photocatalyst. The structure of the semiconductor can be studied the OPLS-2005 forcefield and low mode sampling logarithm [28]. The structures with lower energy window can be optimized by DFT and B3LYP [29]. The optical studies of the material can be calculated by different models of TD-DFT. The redox potential of the catalyst can be calculated by using DFT and TD-DFT with equation $E^{\circ}(x) = -\Delta G(x)/nF$

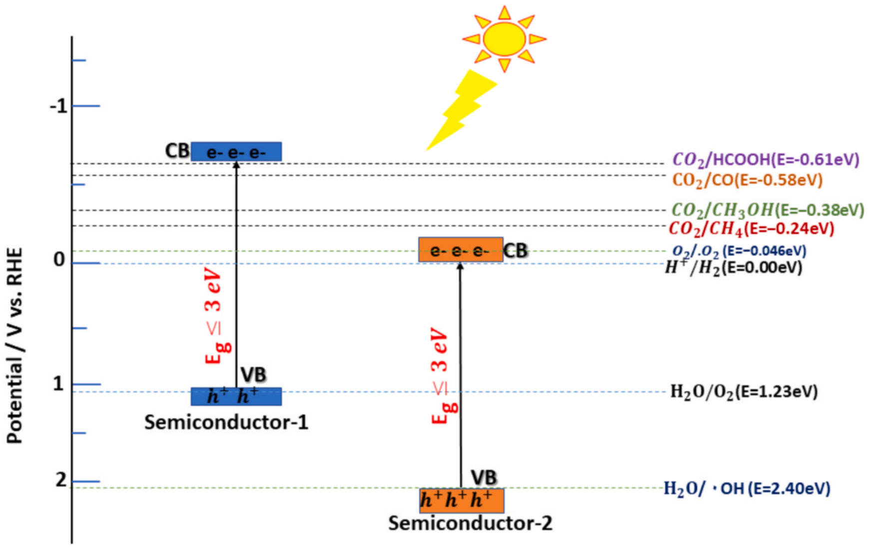

**Fig. 1.** Mechanism of Photocatalytic Water Splitting, Photodegradation of Dye, Photoreduction of $CO_2$ and Photocatalytic $H_2O_2$ production.

[30,31].

There are some factors which affect the activity of the photocatalysts (i) the band structure of the semiconductor catalyst plays an important role to optimize the activity of the catalyst and usually band gap value is lied between 0.2eV-3.5 eV. The ideal value of band gap is typically concentration between 1.23 eV and 3.0 eV. (ii) Charge carrier excitation and separation is crucial part to enhance the photocatalytic activity of the material. When photogenerated charge carriers face any defect in the semiconductor they recombine and release energy due to coulombic forces. Therefore, charge separation is necessary during the development of the catalysts. (iii) the surface activity of the catalyst is also necessary for the favorable activity of the material. The surface activity is determined by quality and quantity of the active sites and surface morphology of the material [32]. Therefore, the design and development of photocatalyst should consider both factors to enhance the activity of the material. There are some methods that can be used to improve the activity of the materials. (1) Adjustment of the band gap structures by modulation of electronic configuration with doping (2) Structural medication of the materials by using significant synthesis method to control the morphology of the catalysts (3) The use of specific cocatalyst which creates of active sites, reduces activation energy of the reaction and provides sufficient system stability (4) Construction of heterojunction typically suppresses the charge recombination and increases the charge separation and considered to be the most effective method to improve the efficiency of the semiconductor photocatalysts [33].

Generally, the heterojunction is an interface between two different semiconductors with unequal band structure leads to spatial band alignments [34,35]. There are three types of conventional heterojunctions: (a) Type-I (b) Type-II (c) Type-III. Type-I heterojunction (Fig. 2a) is known as Stradling gap. For this heterojunction, the conduction band (CB) of the semiconductor A are higher due to its lower work function than CB of the semiconductor B due to its higher work function and the valence band (VB) of the semiconductor A is lower than VB of the semiconductor B. Therefore, under solar light illumination, the electrons accumulate in CB and holes accumulate in VB of semiconductor B. Since, the electrons and holes accumulated on the same semiconductor, the electron-hole pairs cannot be separated effectively due to higher probability of recombination rates and redox reaction takes place at lower reduction and oxidation potential and reducing the redox ability of heterojunction photocatalysts significantly [36]. For Type-II heterojunction (Fig. 2b) or staggered gap, the CB and VB levels of the semiconductor A are higher than the corresponding CB and VB levels of semiconductor B, respectively. As a result, photogenerated electrons will migrate to semiconductor B and holes will transfer to semiconductor A under light illumination leads to electron-hole pair separation. The redox ability of type-II heterojunction will also be reduced because the reduction potential and oxidation potential take place at lower reduction and oxidation potential [37,38]. Although type-II is ideal for charge separation but the charge separation takes place at lower reduction potential which is unfavorable for photocatalytic reactions. As the electrons are accumulated on CB of semiconductor B and holes are accumulated on semiconductor A with weak reduction and oxidation potential leads to impair driving force for specific photocatalytic reactions thermodynamically. Similarly, the repulsion between electron and electrons of both CB and repulsion between holes of both VB impedes the spatial transfer of charge carriers. The electrostatic attraction between electrons and holes hinders the transfer of electrons and holes from one semiconductor to another. So, the charge transfer in type-II heterojunction is hard to predict and fails to separate the electrons and holes spatially. Besides this, the transfer mode weakens the redox ability of the photocatalytic reactions. Type-III heterojunction (Fig. 2c) or broken gap is similar to type-II heterojunction except that the staggered gap becomes so extreme that the band gaps of both the semiconductors do not overlap leads to separation and migration of electron-hole pairs impossible and make it unsuitable for enhancing the separation of electron-hole pairs [39]. Among the conventional heterojunction, type-II heterojunction is the most effective heterojunction to enhance the photocatalytic activity due to its favorable structure for spatial separation of electron-hole pairs. But there are some limitations for the development of type-II heterojunction. As the redox reactions take place with lower reduction and oxidation potentials it suppresses the redox ability of the semiconductor photocatalysts. Moreover, the migration of electrons from semiconductor A to electron rich CB of semiconductor B and holes migrate from semiconductor B to holes rich VB of semiconductor A leads to electrostatic repulsion

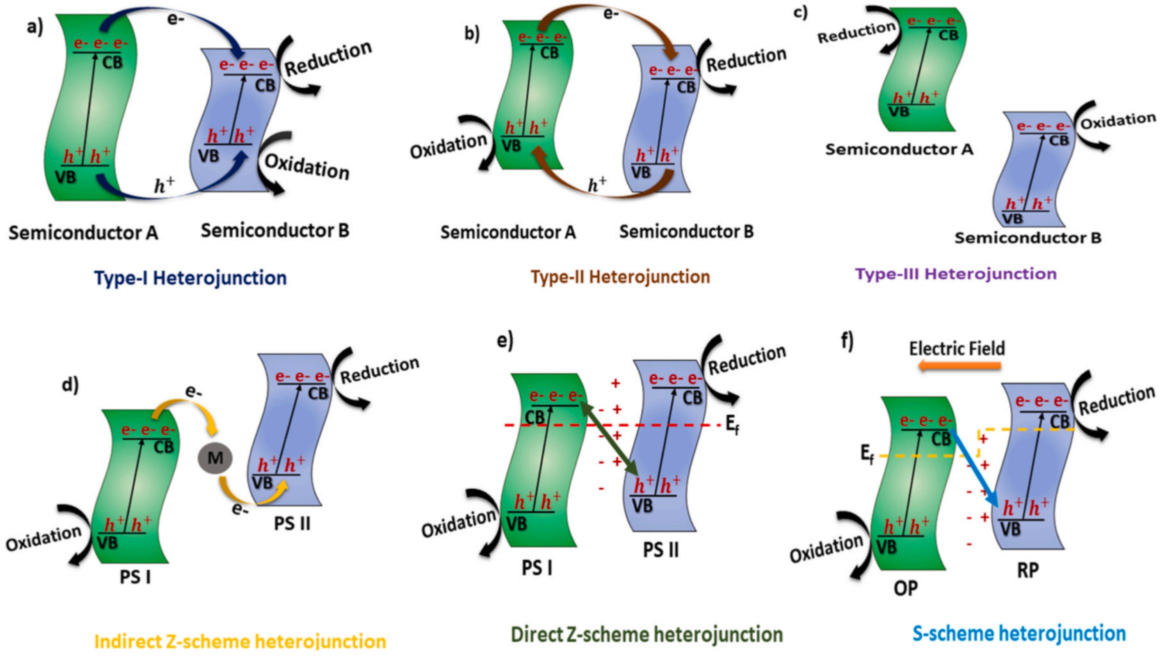

**Fig. 2.** Schematic Illustration of different types of separation of electron-hole pairs in light responsive heterojunction photocatalysts: a) Type-I, b) Type-II, c) Type-III, d) Indirect Z-scheme, e) Direct Z-scheme, and f) S-scheme heterojunctions.

between electrons and electrons as well as holes and holes and make them unfavorable heterojunction. To overcome the aforementioned problem, Z scheme heterojunction was introduced by Bard in 1979 to enhance the redox ability of the heterojunction systems. The conventional Z scheme heterojunction consists of two photocatalyst systems PS I, PS II semiconductors and acceptor/donor (A/D) pairs. During the reactions the electrons from the CB of PS II transfer to the VB of PS I through acceptor/donor pairs. Here, A is reduced to D by reacting with the electrons from the CB of PS II. D is oxidized to A by the holes from VB of PS I. The electrons are accumulated on PS I with higher reduction potential and holes are accumulated on PS II with higher oxidation potential leads to higher redox ability. But it is feasible for liquid mediums only, produces side products, low light harvesting ability and pH sensitivity limiting its applications. Therefore, solid state Z scheme heterojunction (Fig. 2d) was developed in 2006 by Tada in which solid electron mediator was used between PS I and PS II semiconductor systems. Under light illumination, the electrons were transferred from CB of PS II to VB of PS I through electron mediator and electrons and holes are separated at higher reduction potential and oxidation potential with optimized redox ability. It is suitable in solid, liquid ang gas phases for photocatalytic applications [40]. But they faced some problems which are remained unsolved. It is hard to control the synthesis process as the majority of conductor particles does not lie exactly between the photocatalyst and randomly lie on the surface of the photocatalysts. Instead of acting like electron mediator they started to act like cocatalyst. The noble metals are conductors and usually absorb light and starting to compete with the photocatalysts in light harvesting and reduces the light harvesting ability of the photocatalysts. To align the Fermi levels the Schottky barrier is formed between metal and semiconductors and suppresses the flow of electrons from both semiconductors to metal leads to band arises at the interface and asserted charge transfer does not take place. In 2013 Wang group prepared direct Z scheme heterojunction (Fig. 2e) without the solid-state electron mediator. Direct Z scheme has staggered bands which mimics the natural photosynthesis process. This heterojunction consists of two semiconductors PS I and PS II. When both semiconductors with different energy levels come in contact the Fermi levels make an equilibrium. The band edge bending occurs at the interface of both semiconductors and produces electrostatic attraction which accelerates the recombination of electrons of PC I electrons and PC II holes. The electrons in the CB of PC II and holes in the VB of PC I lead to reduction and oxidation of water with higher redox potentials. The main advantages of this type of heterojunction are that electrons and holes are separated at higher reduction and oxidation potentials without expensive electron mediator and cost of the photocatalyst is comparable to type-II heterojunction photocatalysts. Simultaneously, the migration of electrons from CB of PS II to VB of PS I is easier due to electrostatic attraction between electron and hole pairs [41,42]. But the charge transfer mechanism of the direct Z scheme heterojunction lacks experimental evidences and limits its applications. By keeping the idea of direct Z scheme in view the concept of S scheme heterojunction was introduced. The S scheme heterojunction (Fig. 2f) basically consists of two semiconductors reduced photocatalyst (RP) and oxidation photocatalyst (OP). The RP has higher CB, VB, Fermi level and smaller work function than OP. When RP and OP comes in contact the electrons in RP with higher Fermi level will migrate to the OP with lower Fermi level at the interface [43]. The RP loses electrons and becomes positively charged. Meanwhile, the OP gains electrons and becomes negatively charged leads to upward and downward band bending at the interface of OP and RP. Concurrently, a built-in electric field is produced which is directed from RP to OP and photogenerated electrons are transferred from CB of OP to VB of RP under light irradiation [44]. Moreover, the coulombic attraction between electrons of OP and holes of RP and band bending between them favors the charge transfer [45]. Contrarily, coulombic repulsion, band bending and built-in electric field inhibit the electron transfer from the CB of RP to CB of OP. The powerful electrons and holes are reserved in CB and VB of RP and OP and weak charge carriers are recombined leads to strong redox ability. The charge transfer path is step-like macroscopically, therefore named as S scheme heterojunction [46,47]. The main disadvantages od S scheme heterojunctions are: (a) they are limited to powder photocatalysts (b) Their applications in the field of photo electrochemistry are limited (c) They are usually constructed using the n-type semiconductors having suitable band structures and Fermi level positions [48]. The specific conditions are required for the formation of specific types of heterojunctions. They include: (i) Spatial band alignment (ii) Compatible lattice matching (iii) High quality interface with minimal defects with less recombination of charge carriers (iv) Chemical and photo stability (v) Controlled Morphology (vi) Energy level alignments [49]. The common characterization methods to study the formation of heterojunction are X-ray photoelectron spectroscopy (XPS), Kelvin probe force microscopy (KPFM), DFT calculation and electron paramagnetic resonance (EPR). XPS detect the energy density and electron binding energy of both semiconductors using different conditions and parameters. In these methods, under light illumination the hybridization of semiconductors takes place, interfacial charge transfer occurs which increase the electron density and shifting the binding energy of both semiconductors leads to identify the formation of type of heterojunction [50]. Similarly, KPFM measures the surface potentials and corelated the charges on the semiconductors with the Fermi levels [51]. DFT calculations provides the information about work functions and density of states (DOS). Upon charge transfer between the semiconductors charge density difference is produced which shows the accumulation and depletion of electrons in the semiconductor photocatalyst and demonstrates the electron transfer from one semiconductor to other [52,53]. EPR method used radicals which are produced by photoreduction of $O_2$ and photooxidation of water. The higher redox powers stronger will be the EPR signals. Therefore, the composite of semiconductors shows stronger EPR signals than individual semiconductors show the formation of heterojunction and also demonstrate the type of heterojunction [54]. These heterojunctions have various applications: Type-I heterojunction has Efficient charge confinement and suitable for those applications in which electrons and holes should be accumulated in one material. They are applicable for LEDs and Laser diodes. But they have limited charge separation and higher charge recombination. Type-II heterojunction has efficient and spatial charge separation with reduced charge recombination. They are used for photocatalysis, photovoltaics and photodetectors. But they have lower absorption efficiency and interface quality. P-n heterojunction has built-in electric field and can be used in solar cells, photodetectors and diodes. Schottky junctions has efficient charge separation at metal and semiconductor interface and used in Schottky diodes. But they face metal and semiconductor interface have high rate of recombination and have very limited choice of metals.

In this review heterojunction in the metal oxide and metal sulfide-based composites with their various photocatalytic activities are discussed. These composites have following advantages: (a) They have higher surface area which provides more active sites for the reactions. (b) they have optimal band gap (c) Balanced charge separation and transfer upon heterojunction formation (c) Have higher chemical and thermal stability (d) They are abundant in nature, non-toxic and cost effective (e) Higher visible light absorption spectrum and show surface plasmon resonance (SPR) effect [55–57]. The photo electrocatalysts are also discussed with the photocatalysts due to following reasons: (1) photo electrocatalysts incorporate the external electric field which help to separate the charge carriers and reduces the recombination (2) The applied voltage facilitates the better control over the reaction pathways and produces the desired products (3) The external electric field lowers the activation energy of the reactions compared to photocatalytic reactions (4) Help to prevent photo corrosion, increase stability and longevity [58,59]. To be remain focused, authors have emphasized on the mechanistic study of different type of heterojunctions along with some representative applications for in depth investigations. Moreover, some representative examples are also required to correlate and establish the problems associated with the different hetrojunction schemes and to analyze them in exploring the future strategies. Therefore, metal oxide-metal oxide, metal oxide-metal sulfide, and metal sulfide-metal sulfide-based heterojunctions were selected as representative to be remain focused. Otherwise, Metal Carbides, Metal Nitrides, Metal Phosphides and/or other semiconductors may also be included in the review, that may increase the width of the article but the main strategies may remain same. So, the objectives of the review articles were fulfilled by the chosen representative metal oxides and metal sulfides.

This review represents the appreciation of recent efforts and work in constructing various types of heterojunctions in metal oxide based and metal sulfide-based composites and highlights their applications in water splitting, photoreduction of $CO_2$, photodegradation of dyes and photocatalytic $H_2O_2$ production. The above explained four types of heterojunctions and their applications as well as role of nano-pyrophosphate in the catalyst are reviewed. Furthermore, we are suggesting three different kinds of novel schemes of ternary composites in this review which are discussed in the conclusive discussion of each portion and would be helpful to develop novel and highly effective heterojunctions in future. We hope that this review provides useful information on synthesis of various heterojunction in binary and ternary composites of metal oxide and metal sulfide and their applications in photocatalysis.

## 2. Metal oxide-metal oxide based composite

Metal oxides have excellent chemical stability, a wide range of band gaps and suitable band gap positions [60]. Normally, VB and CB of metal oxides have O 2p and transition metal s, p & d characters. The metal oxides in which metals have s orbital and high ionic character 2p have large band gaps. The metals oxides in which metals has $d^n$ electronic configuration possess smaller band gap. By combining these two different kinds of metal oxides binary and ternary oxides are formed with adjustment the band gap position of both metals [61]. All types of mechanisms for adjustment of band gap positions and charge transfer in metal oxide heterojunctions are explained by using representative examples below.

### *2.1. Type-II heterojunction*

The Fermi level, coulombic forces and work functions play an important role to form specific type of heterojunction. The type-II heterojunction consists of two semiconductors. When two semiconductors come in contact the charge transfer takes place to build type-II heterojunction due to difference of Fermi level. The electrons will move from semiconductor with higher Fermi level and lower function to the semiconductor with lower Fermi level and higher work function. The movement of electrons leads to create electric field at the interface due to coulombic forces between the charges and ions of the donor or acceptor atoms. These electric fields cause the energy bands to bend and Fermi levels make an equilibrium forming the staggered band structure [62,63]. Chai et. al., reported a three-dimensional urchin-like photoanode $TiO_2@Fe_2O_3$ was prepared by combination of colloid sphere template, atomic layer deposition and hydrothermal method. The Co-Pi was used as an oxidation co-catalyst showing the significant increase in its photocurrent density from 1.58 mA/cm$^2$ to 3.6 mA/cm$^2$ at 1.23 V and 1.6 V vs RHE (see Fig. 3a-b). The mechanism for electron transfer involves two n-type semiconductors. The band gap of $TiO_2$ and $Fe_2O_3$ is 3.2 eV and 2.2 eV containing CB values of both semiconductors are 0.18 and 0.46 eV and VB values are 3.38 and 2.66 eV. As CB values of $Fe_2O_3$ is more negative and VB values of $TiO_2$ is more positive, than electrons will travel from $Fe_2O_3$ to $TiO_2$ conduction band and holes will travel in opposite directions. In this heterojunction when light falls on photoanode the electrons in the valence band become excited and migrate to conduction band of both semiconductors leaving holes behind (Fig. 3a). The Fermi-level of both semiconductors got adjusted due to internal electric field produced by movement of charge carriers and electrons will travel from CB of $Fe_2O_3$ to $TiO_2$ with lower reduction potential and reach to Pt cathode and cause reduction of water to produce hydrogen. Meanwhile, holes in the VB of $TiO_2$ will travel to VB of $Fe_2O_3$ and quenched by oxidation catalyst Co-Pi and lower overpotential of oxidation of water and increase the oxidation kinetics of $Fe_2O_3/Fe_2TiO_5$ [64].

In the same way, Zhang et. al., synthesized p-n heterojunction of p-CuO ($E_g$=1.34 eV) and n-ZnO ($E_g$=3.14 eV) by combination of one step electrodeposition and thermal treatment methods on cauliflower shaped photocathode. The electrons would travel from p to n semiconductor forming a p-n junction and the type-II mechanism was formed as electrons and holes travel in opposite directions [65]. Pihosh et. al., prepared n-n and type-II heterojunction with $WO_3$ ($E_g$=2.71 eV) nanorods and $BiVO_4$ ($E_g$=2.4 eV) thin layers and co-catalyst Co-Pi by glancing angle deposition and normal physical sputtering on Iodine doped tin oxide (ITO) substrate with photocurrent density of 3.2 and 5.1 mA/cm$^2$ at 1.23 V versus reversible hydrogen electrode (RHE) under simulated

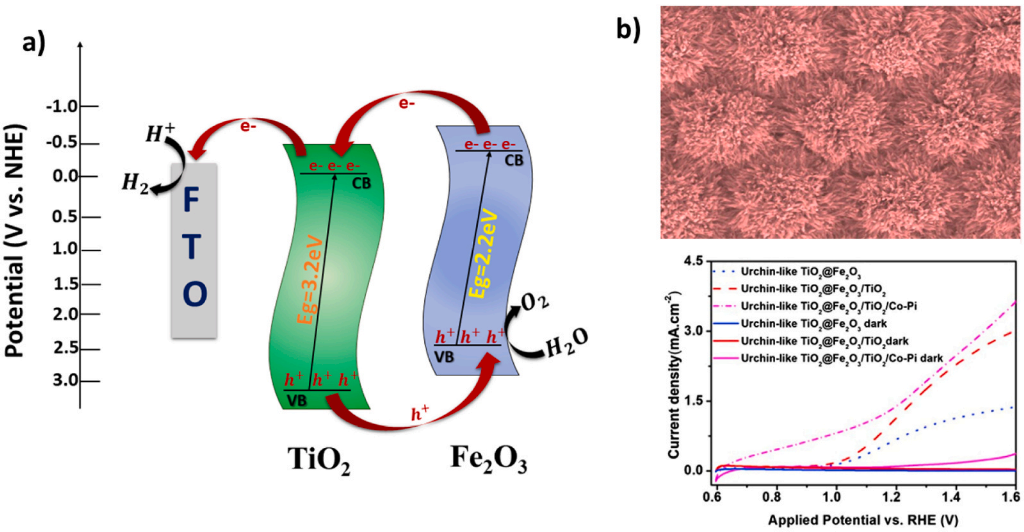

**Fig. 3.** a) Mechanism of charge transfer of $TiO_2/Fe_2O_3$ b) Photocurrent density of Urchin-like TiO2@$Fe_2O_3$ in light & dark. Reproduced with permission and copyright 2018, Elsevier [64].

solar light 100 and 200 mW/cm$^2$ in 0.5 M $Na_2SO_4$ electrolyte [66]. Castro et. al., synthesized $WO_3$ and $TiO_2$ heterostructure by hydrothermal method with different concentrations of $WO_3$ (20 %, 40 %, 80 %) and 40 % hybrid shows highest current density 210 μA/ cm$^2$ and less charge carrier recombination. The electrons would be shifted to CB of $WO_3$ that moves to the Pt cathode for reduction of water and holes in opposite directions, building type-II mechanism [67].

Hao et. al., synthesized a photoanode of n-type $TiO_2$ and p-type $Ag_2O$ ($E_g$ =3.0 eV) by hydrothermal and chemical bath deposition method having photocurrent density 1.61 mA/cm$^2$ at 1.23 V vs. NHE with 0.5 M $Na_2SO_4$ electrolyte under visible light irradiation. The mechanism is p-n and type-II heterojunction [68]. Yao et. al., used chemical bath deposition (CBD) method to synthesize $TiO_2$ and p-$Cu_2O$ ($E_g$=2.1 eV) core/shell nanowire arrays. It showed 2.5 mA/cm$^2$ photocurrent density 2.5 times higher than pure $TiO_2$ nanowires and produced $H_2$ 32 μmol/h$cm^2$ which is 1.7 times higher than pure form. The photoexcited electrons are transferred from CB of $Cu_2O$ to $TiO_2$ and holes in opposite directions representing Type-II mechanism [69]. Wang et, al., organized heterostructure of rutile $TiO_2$ nanorods and Nano bowls (NR@NB) arrays by hydrothermal method forming type-II heterojunction. The photocurrent density was 1.24 mA/$cm^2$ at 1.23 V with RHE two times of bare $TiO_2$ NRs on FTO [70]. Suleiman et. al., synthesized a photocatalyst of $TiO_2$ /ZnO ($E_g$=3.2 eV) by wet chemical method for degradation of azo-dye orange II in water solution which is 53 % under UV light illumination and 72 % under visible light illumination. It is due to higher surface illumination under light, effective charge separation and finer contact which type-II between both semiconductors [71]. Achouri et. al., prepared ZnO/$Fe_2O_3$ heterostructure by wet chemical method (sol-gel method). Iron oxide has narrow band gap (1.9–2.2 eV) and ZnO has broader band gap (3.2 eV) and their composite have better charge separation and increased degradation efficiency of salicylic acid (SA) up to 60 % under UV light exposition in 1 hour [72]. A ternary composite of ZnO/$ZnFe_2O_4$/$TiO_2$ was prepared by hydrothermal method with excellent photocatalytic performances of 96.32 % of methylene blue (MB) degradation due to spatial charge transportation. For the photodegradation OH species produced by visible light irradiation of the photocatalysts are responsible for photodegradation of the contaminants. The CB and VB of the semiconductors should be placed in such a way that reduction potentials of $O_2^-$ and oxidation potentials of OH species are in the scope of the band gaps thermodynamically [73]. ZnO and $TiO_2$ have wider band gap $ZnFe_2O_4$ will be used for degradation and other two semiconductor photocatalysts would contribute individually in the $ZnFe_2O_4$. Under light illumination, electrons will migrate from the VB to the CB of the semiconductors leaving the holes behind in the VB. Because the potential of $ZnFe_2O_4$ is more negative than ZnO and $TiO_2$, the electrons of $ZnFe_2O_4$ will travel to $TiO_2$ and ZnO. This process reduces the recombination of electrons and holes. The electrons react with $O_2$ to form $O_2^-$ radicals. The $O_2^-$ radical reacts with $H^+$ to form $H_2O_2$ and further reacts with electrons to form OH species for degradation process [74]. Iqbal et. al., developed a p-n heterojunction of $ZnFe_2O_4$/$TiO_2$ with (1:1), (1:2) and (2:1) by hydrothermal method with pre-annealing treatment of $ZnFe_2O_4$ at 900℃ and sol-gel method followed by post-annealing of heterostructure at 500℃ for the reduction of $CO_2$ to methanol. The photocatalytic production of methanol is 693.31 μmol (g cat)$^{-1}$ with 1:1 due to lower band gap, higher surface area, more active sites, more crystallinity, maximum visible light absorption, maximum charge separation and transportation for $CO_2$ reduction. Here electrons are transferred from CB of $ZnFe_2O_4$ to $TiO_2$ and holes in opposite direction and reduction potential of methanol is near CB of $TiO_2$ [75].

### 2.2. *Direct Z-scheme Heterojunction*

In the case of direct Z scheme, the backward reactions and shielding effect in the heterojunction are suppressed due to absence of electron mediator. When two semiconductors come in contact the work function difference and formation of electric field are significantly necessary for photogenerated charge separation and transfer [76]. One semiconductor with higher CB and VB and lower work function comes in contact with the semiconductor having lower CB and VB and higher work function leads to formation of internal field and favors Z heterojunction [77]. The factors internal electric field, extra potential barrier induced by band bending and coulombic repulsion inhibit the transfer of electrons from CB of one semiconductor to other. Similarly, the internal electric field also suppresses the transfer of electrons from CB to CB of semiconductors leading to formation of Z scheme heterojunction [78–81]. Zhou et. al., fabricated open bird-nest structured (Fig. 4a) ZnO-$TiO_2$ by hydrothermal approach and controlled spin-coating method to solve problems like poor light harvesting and sluggish carriers' kinetics. The photoanode have photocurrent density 1.05 mA/cm$^2$ at 0.6 V and 2.75 mA/cm$^2$ at 1.23 V vs RHE which 4.32 and 2.27 times higher than $TiO_2$ and 1.98 and 1.38times higher than sealed CS ZnO-$TiO_2$ photoanode. Under the light illumination excitation of electrons took place and transferred from VB to their CB. As the CB value of ZnO is −0.17 eV and that of $TiO_2$ is −0.20 eV then electrons will transfer from more negative to less negative. But the electrons travel from CB of ZnO to VB of $TiO_2$ due formation of Schottky barrier and electrons of $TiO_2$ produced hydrogen with higher reduction potential and holes in the VB of ZnO produced oxygen with higher oxidation potential. So, Schottky junction has managed better charge separation than type-II junction due to reduction and oxidation of water at higher reduction and oxidation potential. Due to the formation of the Z-shape this mechanism is Z (Fig. 4b) mechanisms [82].

Dhiman et. al., synthesized dual function ZnO/$Fe_2O_3$ heterostructure via sol-gel method and spin coating method for degradation of sulfamethoxazole (SMA) and detection of dopamine (DA). The composite degraded SMA upto 95.2 % under visible light exposure in 90 minutes with limit of detection and limit of quantification for $S_2$ modified surface of dopamine is 0.18 μM and 0.62 μM and are calculated as: LOD=3xS/m and LOQ=10xS/m [83]. Chen et. al., synthesized ZnO-$WO_3$ composite by in-situ solvothermal method having 1,5,10 and 15 ratios in which Zn-W-5 under light illumination have lowest onset potential 0.36 V vs. RHE and highest photocurrent density 2.39 mA/cm$^2$ at 1.23 V vs. RHE 2.13 times higher than ZnO NRs and IPCE% up to 84 %. The charge transfer mechanism followed in this composite is solid-state direct z-scheme (Fig. 5a-b) as the band edge of ZnO bend downward and $WO_3$ bend upward cause recombination of electrons and holes. Meanwhile, electrons of ZnO and holes of $WO_3$ cause reduction and oxidation of water. Piezoelectric PEC water splitting is also generated with 300–1000 rpm rate, giving 3.09 mA/cm$^2$ at 1.23 V vs. RHE photocurrent density and 0.21 V lowest onset potential [84].

A ternary photoanode ZnO/AgI/$WO_3$ was developed by hydrothermal method having double direct z-scheme activities and degradation of methylene blue (MB) occurred up to 85.2 % under visible light. PL spectra of ternary composite show lowest emission peaks which means it has lowest recombination of electrons and DRS spectra shows composite has lowest band gap which is 2.79 eV. Here, the Z-scheme shows electron-holes of $WO_3$-CB and ZnO-VB and AgI-CB and WO3-VB recombine while electrons of AgI-CB cause reduction and holes of $WO_3$-VB cause oxidation [85]. CuO quantum dots (QDs)/$WO_3$ NS also formed a direct Z-scheme by self-assembly strategy loading of 0D CuO QDs on 2D $WO_3$ NS [86]. Whereas, a heterostructure of $Cu_2O$ and $TiO_2$ with direct Z-scheme heterojunction was reported by solvothermal method and stabilizing $Cu_2O$ from photo corrosion to reduce $CO_2$ to methanol and ethanol. The photocatalytic conversion of $CO_2$ to CO is 2.11μmol (g cat)$^{-1}$ four times higher than pure $Cu_2O$. The band alignment and energy differences at the interface of the composite are usually determined by XPS and DRUV. If the composite follows the Type-II (staggered gap) band, the energetic CB favors the reduction of $CO_2$ via photogenerated electrons. After considering the energy difference between CB and Fermi level of $TiO_2$ as well as VB and Fermi level of $Cu_2O$ do not remain constant before and after contact. The energy difference

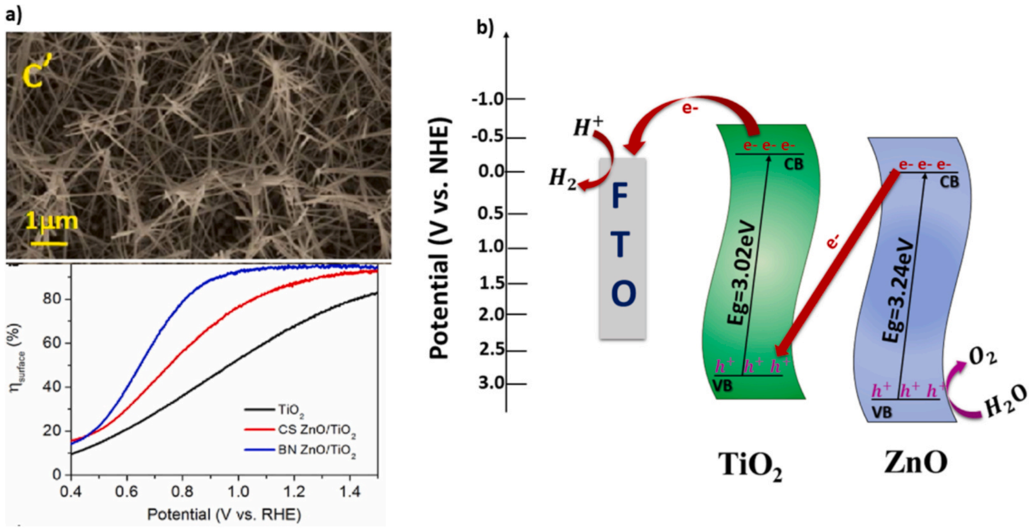

**Fig. 4.** a) Open bird nest structured $TiO_2$/ZnO b) Mechanism of charge transfer of $TiO_2$/ZnO. Reproduced with permission [82]. Copyright 2014, Elsevier.

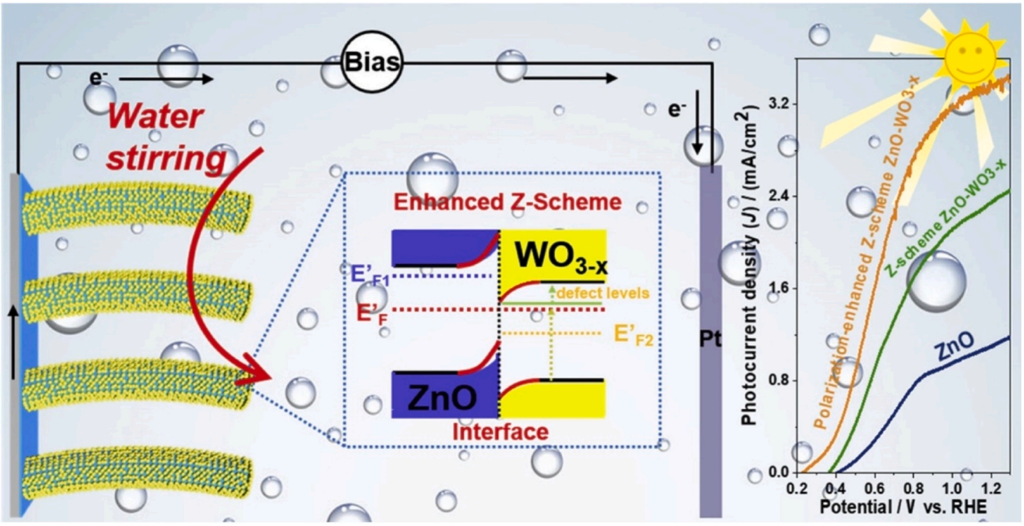

**Fig. 5.** Schematic diagram of polarization process of ZnO and PE-PEC process with energy band diagram of Zn-W-m. Reproduced with permission [84]. Copyright 2019, Elsevier.

between the CB of $TiO_2$ and VB of $Cu_2O$ before contact is 0.62 eV. This energy difference between the CB of $TiO_2$ and VB of $Cu_2O$ is favorable for separation of photogenerated electron and hole pairs through direct Z scheme heterojunction due to overlap of energy levels upon p-n heterojunction formation. In order to make the reduction of $CO_2$ feasible, Z scheme pathway is followed and anodic reaction takes place in the $Cu_2O$ surface as CB level of $Cu_2O$ is less negative than $CO_2$ reduction potential. So, to make $CO_2$ reduction thermodynamically possible holes are scavenged by water because accumulation of electrons in CB of $Cu_2O$ leads to production of CO [87].

### *2.3. Indirect Z-scheme Heterojunction*

In this type of heterojunction electron mediator (Ag, Au and Pt) is used between the two semiconductors reduce the charge transfer length and accelerate the charge transfer. It consists of three components and the Fermi level of one semiconductor is higher than other semiconductor with lowest Fermi level of the metal mediator. All three components come in contact and charges redistribute at the interface having different Fermi levels. To align the Fermi levels, the electrons will transfer from both semiconductors to the metal surface. Simultaneously, band bending takes place at the interface of semiconductor and metal forming the Schottky barrier and suppress the flow of electrons from both semiconductors to metal. Therefore, electrons with lower CB transfer to metal and recombine with the holes of VB of another semiconductor [42,88,89]. Tahir et. al., prepared a solid-state Z-heterojunction consisting of $ZnFe_2O_4$ ($E_g$=1.99 eV), Ag and $TiO_2$ photocatalysts by hydrothermal, photo-deposition and solvothermal method (Fig. 6a-b). The photocatalytic activity of nanocomposite was improved by fabrication of Ag nanoparticles as electron mediator and obtained highest CO amount of $1025 \mu mol g^{-1} cat^{-1}$ and hydrocarbons like $CH_4$, $CH_3OH$ and $C_2H_6$ with amount of 132, 30.8 and $19.1 \mu mol g^{-1} cat^{-1}$(Fig. 6b). Under light illumination, the electrons got excited by absorption of photons and migrated from their VB to CB. The CB of $TiO_2$ is much lower than CB of $ZnFe_2O_4$ and close to VB of $ZnFe_2O_4$ and Ag in between act as electron mediator. The electrons from CB of $TiO_2$ would transfer through Ag forming an Ohmic barrier to VB of $ZnFe_2O_4$ and cause reduction and holes in VB of $TiO_2$ cause oxidation of $CO_2$ to form CO and $CH_4$ (Fig. 6a) [90].

A ternary nanostructure of $\alpha$-$Fe_2O_3$/Au/$TiO_2$ photoanode was

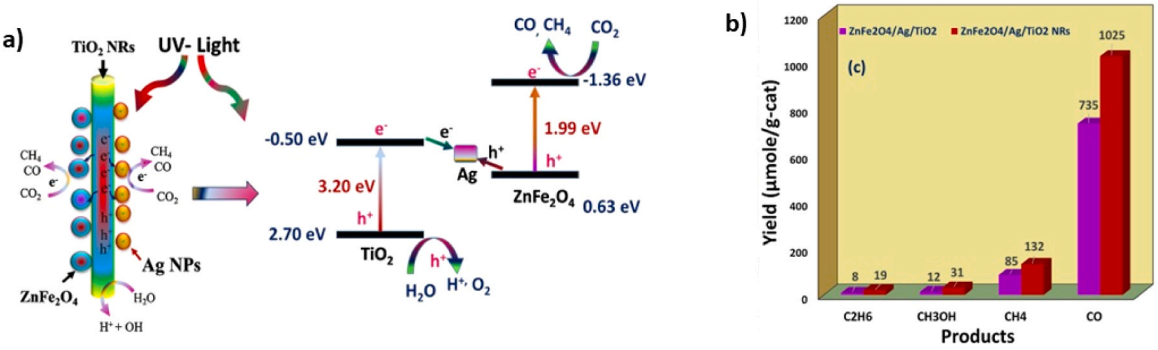

**Fig. 6.** a) Schematic representation of charge transfer in $ZnFe_2O_4$/Ag/$TiO_2$ nanocomposite, b) Performance comparison of nanoparticles and nanorods of nanocomposite catalyst. Reproduced with permission [90]. Copyright 2019, Elsevier.

developed by hydrothermal and pulsed laser deposition method giving photocurrent density 1.05 mA/$cm^2$ at 1.23 V vs. RHE which is 4.2 times greater than bare α-$Fe_2O_3$. This increase in photocatalytic activity is due to formation of heterojunction between $Fe_2O_3$ and $TiO_2$ by Au noble metal which acts as electron mediator and making it a solid state Z-scheme heterojunction [91]. Also, a solid-state z scheme heterojunction of $TiO_{2-x}$/Cu/ZnO was synthesized by atomic layer deposition (ALD) and spray pyrolysis method. In this process, upon light illumination, the incident light penetrates through the ZnO layer and stimulated the electrons from its VB to the CB and the incident light is transformed to scattered light. If the ZnO layer is not present then most of the incident light is bled off but the incident light is repeatedly scattered between ZnO layer and Cu/$TiO_2$ layer. The scattered light from ZnO layer is stimulates the Cu nanoparticles and electrons are generated from resonance collective oscillation. The band gap energy values of ZnO and $TiO_2$ were calculated which clearly demonstrated that the electrons will transfer from CB of $TiO_2$ to Cu as the Fermi level of Cu is more positive than CB of $TiO_2$. Similarly, the Cu metal acts as trap and electron mediator to capture electrons and facilitate the strong electron delocalization. The Fermi level of Cu is lower than VB of ZnO the trapped electrons will eventually be transferred from Cu to the VB of ZnO and holes of ZnO will be quenched. In this way, the photogenerated electrons and holes are separated and reduction of ZnO electrons takes place to produce hydrogen with higher reduction potential ability that led to formation of solid-state Z scheme heterojunction mechanism. Noticeably, the surface plasmon resonance (SPR) effect of Cu between $TiO_2$ and ZnO enhances photocatalytic production of hydrogen which is 342.0 µmol$g^{-1}h^{-1}$ [92]. Similarly, a heterostructure of $Ag_2O$/Ag/amorphous-$TiO_2$ exhibited solid-state or indirect Z scheme by using stober method and stirring. It shows enhanced photocatalytic activity of nitrogen dioxide with photocurrent value of 28.2 nA. The mechanism involves migration of electrons from CB of $Ag_2O$ to Ag making Schottky barrier and finally to VB of $TiO_2$ and electrons in CB of $TiO_2$ cause reduction and holes of $Ag_2O$ cause oxidation of water due to surface plasmon resonance effect (SPR) of Ag between $TiO_2$ and $Ag_2O$ [93]. While, Ag-$Fe_2O_3$-$TiO_2$ heterojunction was developed for photocatalytic degradation of organic dye Rh B by condensation reflux and mild-hydrolysis hydrothermal method. Ag showed localized SPR effect having highest apparent kinetic constant at 0.027$min^{-1}$ with recombination of electrons of $TiO_2$ and holes of $Fe_2O_3$ through Ag. The electrons in CB of $Fe_2O_3$ show reduction and holes of VB of $TiO_2$ show oxidation [94].

### 2.4. S-scheme Heterojunction

A step scheme heterojunction has OP and RP with staggered band structure but a completely different charge transfer route than type-II heterojunction. The electrons are accumulated in the CB of RP and holes in the VB of OP and useless electrons and holes of OP and RP are recombined. RP has a higher CB and smaller work function than OP. When both semiconductors come in contact, the electrons in the RP diffuse into OP creating the depletion layer and accumulation layer at the interface [95,96]. Concurrently, the internal electric field directed from RP to OP and electrons are transferred in opposite directions [97]. When both semiconductors come in contact the Fermi level form a curved shape and band bending occurs for transfer of electrons from CB of OP to VB of RP to recombine under the columbic attraction between electrons and holes [98–100]. An S-scheme based photoanode of 2D/2D $TiO_2$ and $Bi_2O_3$ was established by using hydrothermal methods. Where, the face to face minimized the distance for migration of charge carriers which is very helpful for production of $H_2$ 12.08µmol/g/h (Fig. 7a-b) by extending the lifetime of charge carriers with strong redox abilities. The charge transfer mechanism between 2D/2D $TiO_2$/$Bi_2O_3$ photocatalysts is carried out by keeping one semiconductor as Reduction Photoanode (RP) and another as oxidation photoanode (OR). The band gap of $TiO_2$ is 3.2 eV with conduction band value and valence band values as 0.05 eV and n-type semiconductor. The band gap of $Bi_2O_3$ is 2.72 eV having CB and VB values as 0.02 eV and 2.70 eV and act as n-type semiconductor. Under light illumination the electrons in the VB of both semiconductors became excitation and migrated from VB to their CB. The Fermi-level of both semiconductors is below CB and comes in equilibrium due to formation of interface and internal electric field. The electrons travel from CB of $Bi_2O_3$ to VB of $TiO_2$ to remove non-beneficial electrons and holes while the electrons in the CB of $TiO_2$ reduce water to $H_2$ with higher reduction potential. The holes in VB of $Bi_2O_3$ oxidize water to $O_2$ with higher oxidation potential (Fig. 7a). Here the type-II mechanism is not followed because it does not separate the useless electrons and gives lower activity with reduced redox potential. So the mechanism which followed to increase the production of $H_2$ in s-scheme heterojunction [101].

The photogenerated electrons in CB of $ZnMn_2O_4$ and holes in the VB of ZnO are useful and cause reduction and oxidation with higher reduction potential and higher oxidation potential showing S-scheme mechanism [102]. Another S-scheme based ZnO/$WO_3$ heterojunction showed highest photocatalytic activity of 6788 µmol/Lh of the $H_2O_2$ and sequentially 2.57 mA/$cm^2$ photocurrent density was observed. The electrons after excitation of $WO_3$ recombines with holes of ZnO leaving the electrons of ZnO for reduction of $O_2$ leads to $H_2O_2$ formation while holes of $WO_3$ causes oxidation (same as shown in Fig. 4a). To get the in-depth understanding of photogenerated charge carriers transfer in the S-scheme heterojunction, electron paramagnetic resonance (EPR) measurement was studied by using 5,5-dimethyl-1-pyrrolidine N-oxide (DMPO) as a radical trapper. It is observed that DMPO-.$O_2^-$ signals of ZnO are stronger than $WO_3$ because the electrons on the CB of ZnO hava stronger reduction potential than $WO_3$. Similarly, PL spectra clearly depicts that the composite has smaller wavelength than the ZnO and $WO_3$ shows that the photogenerated charge carriers have low recombination and higher charge carrier separation in the composite. The weaker signals of PL are caused by the combination of less powerful

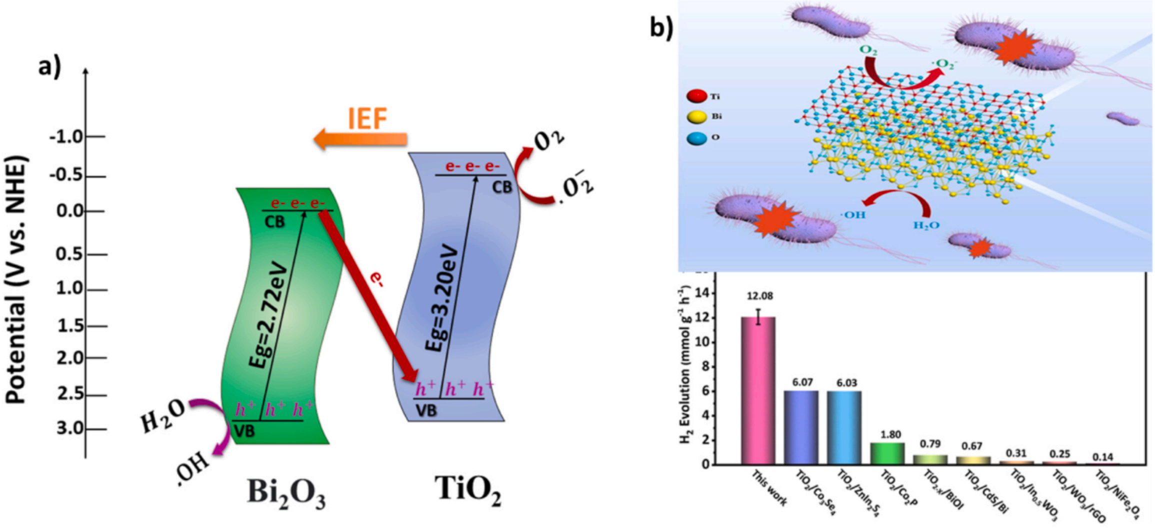

**Fig. 7.** a) Mechanism of charge transfer of $Bi_2O_3$ and $TiO_2$ b) Production of $H_2$ at different concentrations of $TiO_2/Bi_2O_3$. [101]. Copyright 2022, Elsevier.

electron and hole pairs in the composite within S scheme heterojunction. The higher separation of charge carrier efficiency and photosensitivity of the $ZnO/WO_3$ composite could be attributed to formation of S scheme heterojunction and enhance the production of $H_2O_2$ which is 6788 μmol $L^{-1}$ $h^{-1}$ [103]. Also, $WO_3/Ag/ZnO$ by spray pyrolysis technique showed s-scheme heterojunction with Ag as an electron mediator. The composite provides degradation of cephalexin (CPX) up to 98.8 % at rotational speed of 180 rpm and solution flow rate is 1.0 L/min with light intensity 11 mW/$cm^2$ at pH 6. Upon photoexcitation, internal electric field is produced making Fermi-level at equilibrium which causes recombination of electrons of $Ag/WO_3$ and holes of ZnO while reduction $H_2O$ to OH radical occurs by electrons of ZnO cause degradation of CPX and holes of $Ag/WO_3$ causes oxidation involves in other degradations [104]. Similarly, a ternary nanocomposite of ZnO-$V_2O_5$-$WO_3$ in Fig. 8 showed dual s-scheme mechanism having highest photocatalytic activities due to useful electrons of ZnO and $V_2O_5$ and holes of $WO_3$ for reduction and oxidation at their surface active sites. The Raman studies showed that composite has oxygen vacancies that support fast charge separation and lower recombination, and UV-Visible studies showed the band gap of the composite was 2.63 eV. Furthermore, the photocatalytic activity was measured by degradation of cresol red (CR), rhodamine B (RB), methyl orange (MO), safranin-O (SO) and methyl red was 67.0 %, 86.6 %, 98.0 %, 98.0 %, 76.8 % and 99 % under visible light [105].

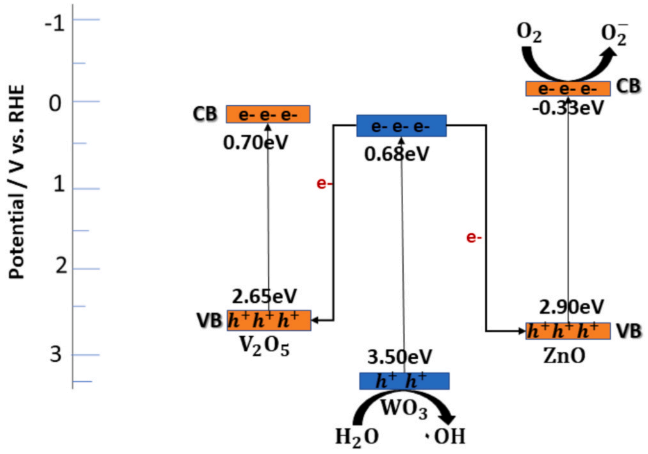

**Fig. 8.** Schematic representation of Dual S-scheme heterojunction in ZnO-$V_2O_5$-$WO_3$ ternary composite. Reproduced with permission [105]. Copyright 2021, Elsevier.

Dual s-scheme heterojunction of $Ga_2O_3/ZnO/WO_3$ was synthesized by electrospinning method for degradation of Rh B. The photoexcited useless electrons of ZnO and $WO_3$ are captured and electrons in the CB of $Ga_2O_3$ with band gap 4.9 eV involve in reduction while holes of $WO_3$ involve in oxidation which increases photocatalytic degradation of Rh B [106]. Floatable composite photocatalysts are synthesized by immobilizing the $TiO_2$ and $Bi_2O_3$ on a light weight polystyrene sphere via hydrothermal and photodeposition methods. This floatable photocatalyst is solar transparent and enhances the contact between reactants and photocatalysts. The photocatalyst produces an enhanced yield of $H_2O_2$ about 1.15 mM $h^{-1}$ by following the step scheme mechanism between $TiO_2$ and $Bi_2O_3$ [107].There are a number of reasons which cause it to increase the activity of the binary or ternary composite. They include specific surface area of host layer, charge carrier diffusion distance, light harvesting efficiency, charge transfer and separation ability, presence or absence of co-catalyst, morphology of host layer, thickness of the guest layer which decides distance which is required for charge carriers to transfer from one layer to other, synthesis method, type of electrolyte, SPR effect of co-catalyst if used, band alignment, band gap, adjustment of Fermi-levels, type of formation of heterojunction. From above explained examples $WO_3/BiVO_4$ (p-n heterojunction) formed by glancing angle deposition and normal physical sputtering shows highest photocurrent density 5.16 mA/$cm^2$ at 1.23 V vs. RHE. It is due to vertical grown $WO_3$ NRs and very low thickness of capped $BiVO_4$ on nanorods, ALD method to produce $BiVO_4$ nanoparticles which reduce the distance between both layers to enhance the charge transfer. Formation of p-n junction for charge separation and SPR effect of co-catalyst Co-Pi. $ZnO/Ag/WO_3$ gives highest degradation percentage of organic dye (CPX) which is up to 98.8 % due to formation of S-scheme heterojunction, increase of surface roughness after loading of $Ag/WO_3$ loading leads to more charge transfer for degradation of dye, increase in hydrophilicity of ZnO layer for surface enhancement to absorb CPX on the surface and SPR effect of Ag which increases the transfer of charges for photo-degradation. After discussion of several mechanisms, an insightful mechanism is inclined for charge transfer in ternary composite which might be helpful to further enhance the activity of metal-based composites like; metal oxide, metal sulfide, metal nitrides, metal carbides (Fig. 9). In Fig. 9, proposed scheme consists of three semiconductor catalysts listed as: semiconductor-1, semiconductor-2 and semiconductor-3. The band gap and band alignment of all semiconductors can be adjusted and band gap of semiconductor-1 may be less than or equal to 3.2 eV, semiconductor-2 may be less than or equal to 2.0 eV and semiconductor-3 may be less than or equal to 2.5 eV. After these adjustments there is a discussion of the mechanism of charge

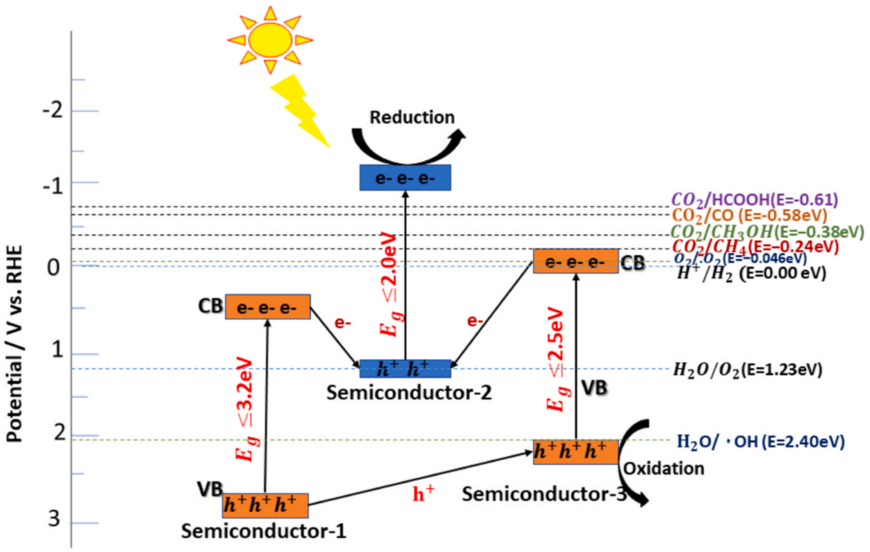

**Fig. 9.** Schemes for semiconductors with different band alignments for transfer of charge carriers.

**Table 1**
Metal oxide-metal oxide heterojunctions for Photocatalytic applications.

| Photocatalysts-Sensitizers | Synthesis Methods | Heterojunction | Activities | References |
|---|---|---|---|---|
| $TiO_2$-$Fe_2O_3$ | Hydrothermal-ALD | Type-II | 3.6 mA/$cm^2$ Photocurrent density at 1.23 V vs. RHE | [64] |
| $WO_3$-$BiVO_4$ | Glancing angle deposition-Normal physical sputtering | Type-II | 5.16 mA/$cm^2$ Photocurrent density at 1.23 vs. RHE | [66] |
| $TiO_2$-$WO_3$ | Hydrothermal-Hydrothermal | Type-II | 0.216 mA/$cm^2$ Photocurrent density at 1.2 V vs. RHE | [67] |
| $TiO_2$-$Ag_2O$ | Hydrothermal-CBD | Type-II | 1.616 mA/$cm^2$ Photocurrent density at 1.23 V vs. NHE | [68] |
| $TiO_2$-$Cu_2O$ | CBD-CBD | Type-II | 2.56 mA/$cm^2$ Photocurrent density at 1.23 V vs. RHE | [69] |
| $TiO_2$ NRS- $TiO_2$ NBs | Hydrothermal-Hydrothermal | Type-II | 1.246 mA/$cm^2$ Photocurrent density at 1.23 V vs. NHE | [70] |
| $TiO_2$ NWs- ZnO | Wet chemical method-Wet chemical method | Type-II | O II degradation –53 % under UV and 72 % under visible light | [71] |
| $Fe_2O_3$-ZnO | Sol gel-spin coating | Type-II | SA degradation 64 % under UV light | [72] |
| ZnO-$ZnFe_2O_3$-$TiO_2$ | Hydrothermal-Hydrothermal-Hydrothermal | Dual type-II | Degradation of MB up to 96.32 % | [74] |
| $ZnFe_2O_4$-$TiO_2$ | Hydrothermal-Sol gel | Type-II | Reduction of $CO_2$ to methanol is 693.31 µmol (g cat)$^{-1}$ | [75] |
| $TiO_2$-ZnO | Hydrothermal-Spin-coating | Direct Z-scheme | 2.756 mA/$cm^2$ Photocurrent density at 1.23 V vs. RHE | [82] |
| ZnO-$Fe_2O_3$ | Spin coating-Sol gel | Direct Z-scheme | SMA degradation 95.2 % under visible light and DA sensing is 0.18 µM | [83] |
| ZnO-$WO_3$ | Solvothermal-Solvothermal | Direct Z-scheme | 3.38 mA/$cm^2$ photocurrent density at 1.23 V vs. RHE with 1000 rpm | [84] |
| CuO-$WO_3$ | Self-assemble method – self-assemble | Direct Z-scheme | Production of 1.58µmol/g/h CO from $CO_2$ | [86] |
| ZnO-AgI-$WO_3$ | Hydrothermal-Hydrothermal-Hydrothermal | Double direct Z-scheme | 85.2 % rate of MB degradation | [85] |
| Cu2O-TiO2 | Solvothermal-Solvothermal | Direct Z-scheme | Photoreduction of $CO_2$ to CO is 2.11µmol (g cat)$^{-1}$ | [87] |
| $ZnFe_2O_4$-Ag-$TiO_2$ | Solvothermal-photo deposition-Hydrothermal | Solid state Z-scheme | Production of CO, $CH_4$, $CH_3OH$ and $C_2H_6$ is 1025, 132, 30.8 and 19.1µmolg$^{-1}$$cat^{-1}$ | [90] |
| α-$Fe_2O_3$-Au-$TiO_2$ | Hydrothermal-Pulsed laser deposition-Hydrothermal | Solid state Z-scheme | 1.05 mA/$cm^2$ Photocurrent density at 1.23 V vs. RHE | [91] |
| $TiO_2$-Cu-ZnO | Hydrothermal-ALP-Spray pyrolysis | Solid state Z-scheme | Production of $H_2$ is 342.0µmol/g/h | [92] |
| $Ag_2O$-Ag-$TiO_2$ | Stober Method-Stober Method-Hydrothermal | Solid state Z-scheme | Photocurrent production is 28.2 nA | [93] |
| Ag-$Fe_2O_3$-$TiO_2$ | Condensation reflux method-Hydrothermal | Solid state Z-scheme | Highest kinetic constant value 0.027min$^{-1}$ for degradation of Rh B | [94] |
| $TiO_2$-$Bi_2O_3$ | Hydrothermal-Hydrothermal | S-scheme | Photocatalytic $H_2$ production 12.08µmol/g/h | [101] |
| ZnO-$ZnMnO_4$ | Electrospinning-Electrospinning | S-scheme | 1.06 mA/$cm^2$ Photocurrent density at 1.23 V vs. RHE | [102] |
| ZnO-$WO_3$ | Hydrothermal-Hydrothermal | S-scheme | 6788 µmol L$^{-1}$ h$^{-1}$ $H_2O_2$ production | [103] |
| ZnO/Ag/$WO_3$ | Spray pyrolysis - Spray Pyrolysis -Spray pyrolysis | S-scheme | Degradation of CPX 98.8 % | [104] |
| ZnO-$V_2O_5$-$WO_3$ | Electrospinning-Electrospinning-Electrospinning | Dual S-scheme | Degradation of CR, RB, MO, SO and MB is 67 %, 86.6 %, 98.0 %, 76.8 % and 99.0 % | [105] |
| $Ga_2O_3$-ZnO-$WO_3$ | Electrospinning-Electrospinning-Electrospinning | Dual S-scheme | Degradation of Rh B | [106] |
| $TiO_2$-$Bi_2O_3$ | Hydrothermal-Photo-deposition | S-scheme | 1.15 mM h$^{-1}$ $H_2O_2$ | [107] |

separation, migration and reactions on CB and VB of semiconductor catalysts. Under light illumination the electrons in the VB of all semiconductors absorb photons and get excited and migrate to their CB. The migration of charge carriers causes an interface between them and the type of interface tells the route of charge transportation. In this heterojunction the electrons from the CB of semiconductor-1 and semiconductor-3 may transfer to VB of semiconductor-2 for recombination while holes from VB of semiconductor-1 may migrate to VB of semiconductor-3. The photoexcited electrons in the CB of semiconductor-2 at higher reduction potential causes reduction and holes in the VB of semiconductor-3 causes oxidation. It can be explained by taking an example. Consider semiconductors 1, 2,3 as three layers of metal oxides (MO-1, MO-2, MO-3) and the percentage compositions of each layer could be adjusted as MO-1 is 25 %, MO-2 is 40 % and MO-3 is 35 %. As MO-1 layer has larger band gap then it can make the composite stable from photo corrosion in the presence of light and its electrons may not participate in any reaction as CB is below zero potential and recombine with holes of MO-2 layer. MO-3 layer is 35 % because its band gap is less than and equal to 2.5 eV and its CB is above zero potential and different kinds of reactions can take place here such as; $CO_2$ reduction, water splitting and dye degradation under sunlight. MO-2 layer may be 40 % and smaller band gap because there can be lot of reactions occurring in its CB like; $CO_2$ reduction to HCOOH, CO, $CH_3OH$, $CH_4$ and dye degradation and water splitting to produce hydrogen. At the end it is inferring that this scheme can be used for any kind of ternary composite by adjusting the percentage of each layer and can be used for any kind of reaction and for one reaction or more than one reaction at a time.

## 3. Metal oxide-metal sulfide based composites

Metal oxides are used for refining and decomposing wastes and organic substances due to their chemical, physical and optical properties [108]. When the grain size of metal oxides is decreased new possibilities are opened, especially in photocatalysis because as the size decreases, the active sites on the surface of metal increase as compared to their bulk size. Metal oxides form photocatalysts which are enriched enough to absorb light and have compatible and stable morphology, reusable and have large surface area [109]. Metal sulfide photocatalysts are cost effective and ecofriendly and can split water into oxygen and hydrogen. Metal oxides have a wide band gap due to 2p orbitals of oxygen and their localized 2p holes. In contrast, metal sulfides have open exposure of active sites, strong catalytic and photocatalytic abilities, narrow band gap, a suitable band position and utilize a wide solar spectrum. Synthesis of metal oxide and metal sulfide make them effective semiconductor photo electrocatalysts [110].

### 3.1. Type-II heterojunction

The $H_2$ evolution of $ZnIn_2S_4/AgFeO_2$ photoanode is 9.14 μmol/h/g (Fig. 10a-b) at 3 % content of $AgFeO_2$ which is approximately 30 times higher than pure $ZnIn_2S_4$ (0.31 mmol/gh). $ZnIn_2S_4$ and $AgFeO_2$ photocatalysts are n and p type semiconductors, respectively. The VB and CB values of $AgFeO_2$ are 1.69 eV and −0.08 eV and VB and CB values of $ZnIn_2S_4$ are 1.89 eV and −0.61 eV. The Fermi-level values of $ZnIn_2S_4$ and $AgFeO_2$ are approximately −0.65 and 1.25 V (vs SCE) which are calculated by Nernst equation: $E_{NHE} = E_{SCE} + 0.224$. Before contact $E_f$ of $ZnIn_2S_4$ is more negative than valence band potential and $E_f$ of $AgFeO_2$ is more positive than conduction band potential. After loading $AgFeO_2$ nanoparticles on the $ZnIn_2S_4$ microsphere, a p-n heterojunction is formed at their contact interface. Due to different values of Fermi-level between two components electrons will migrate from p-type to n-type semiconductors until the Fermi-levels of both components attain equilibrium. Meanwhile, the VB of $AgFeO_2$ increases with $E_f$ and CB of $ZnIn_2S_4$ decreases with $E_f$. The internal electric field is formed from $ZnIn_2S_4$ towards $AgFeO_2$ after the contact and CB position of $AgFeO_2$ will be more negative than the CB position of $ZnIn_2S_4$. Upon light irradiation electrons and holes are generated. The electrons of both semiconductors migrate from VB to CB leaving the holes behind. Due to synergistic effects of internal force electrons can easily travel from CB of $AgFeO_2$ to CB of $ZnIn_2S_4$ and then these electrons reduce $H_2O$ into $H_2$ and holes travel from VB of $ZnIn_2S_4$ to VB of $AgFeO_2$ and consumed by sacrificial agent. The mechanism in which electrons travel from CB of p-type semiconductor to n-type semiconductor and holes travel from VB of n-type semiconductor to VB of p-type semiconductor are Type-II mechanisms (Fig. 10a-b), indicating Type-II scheme mechanism [111].

Also, a three-dimensional $CdIn_2S_4$ ($E_g$=2.53 eV) deposited over $TiO_2$ photoanode showed the photocurrent density of 3.8 $mA/cm^2$ at 0.2 V vs. Ag/AgCl under AM1.5 solar light illumination that is three times of bare $TiO_2$. Electrons in CB of $CdIn_2S_4$ migrate to CB of $TiO_2$ and then to FTO and cause reduction and holes travel in opposite directions causeing oxidation and giving n-n based type-II mechanism [112]. Moreover, 2D $ZnIn_2S_4$ nanosheets ($E_g$=2.91 eV) and 1D $TiO_2$ nanorods heterojunction was developed that showed photocurrent density of 1.2 $mA/cm^2$ at G1.5AM illumination and 1.5 V vs. RHE that is 3 times higher than bare $TiO_2$ nanorods with onset potential reduced significantly from 0.05 V to −0.53 V. This negative shift of onset potential shows large accumulation of electrons in the heterojunction and decreased charge recombination, evidencing n-n based type-II heterojunction [113]. A type-II heterojunction of 3D rosette-rode $TiO_2/Bi_2S_3$ was developed and showed photocurrent density of 3.98 $mA/cm^2$ at 1.23 V vs. NHE using $Na_2SO_3$ and $Na_2S$ as electrolyte under 100 $mWcm^2$ solar light illumination that is 10 times higher than rutile $TiO_2$ NRs and 5.5 times higher than RT-$Bi_2S_3$ photoanode synthesized via without seeding layer. As the conduction

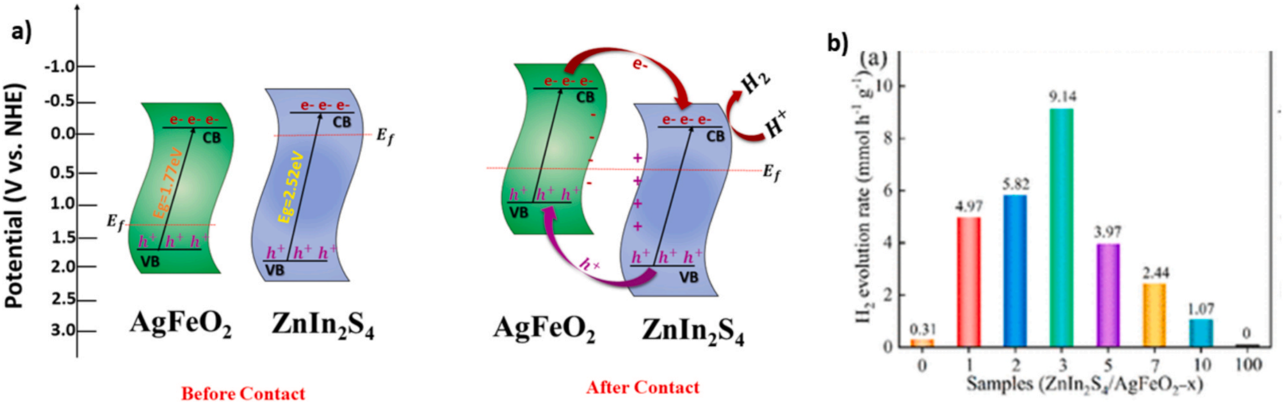

**Fig. 10.** **a) Photocatalytic mechanism for *$ZnIn_2S_4/AgFeO_2$*** composite through p-n heterojunction under visible-light irradiation b) Photocatalytic $H_2$ evolution rate. Reproduced with permission [111]. Copyright 2021, American Chemical Society.

band of $Bi_2S_3$ is more negative then electrons would migrate from CB of $Bi_2S_3$ to CB of $TiO_2$ to FTO and cause reduction while holes travel in opposite direction and cause oxidation of sacrificial agent [114]. Also, $Sb_2S_3$ ($E_g$ =1.7 eV) over $TiO_2$ heterojunction showed photocurrent density of 9 mA/$cm^2$ at −0.4 V vs RHE in 1 M sulfuric acid solution under 1 sun illumination. From X-ray photoelectron spectroscopy (XPS) band alignment studies and bias-dependent incident-photon conversion efficiency (IPCE) shows that $Sb_2S_3$ is weakly n-type, has short diffusion length and large CBO of heterojunction and can be improved by buffering with $In_2S_3$ by reducing CBO, higher CB position and higher onset potential which is 0.25 V. If its mechanism was studied, its electrons would travel from CB of $Sb_2S_3$ to CB of $TiO_2$ under light illumination and holes travel from VB of $TiO_2$ to VB of $Sb_2S_3$ cause reduction and oxidation exhibiting type-II heterojunction [115]. Similarly, β-$In_2S_3$ is sensitized over $TiO_2$ by spin coating and hydrothermal method at different temperatures as $TiO_2/In_2S_3$-(6, 8, 10, 12 and 14). $TiO_2/In_2S_3$-12 showed highest photocurrent density 0.1256 mA/$cm^2$ at 0 V vs. saturated calomel electrode (SCE). After migration of photoexcited electrons the Fermi-levels of both photocatalysts come in equilibrium due to interfacial contact. Electrons transfer from CB of $In_2S_3$ to CB of $TiO_2$ by passing the interface (CB of $In_2O_3$) to FTO substrate and holes travel in opposite directions for reduction and oxidation and form type-II mechanism [116]. Heterojunction of α-$Fe_2O_3/Bi_2S_3$ showed photocurrent density 2.550 mA/$cm^2$ at 1.23 V vs RHE 20 times higher than pristine α-$Fe_2O_3$. EIS showed that sample prepared in 6 h has lowest $R_p$(180.9 Ω$cm^2$), indicating enhanced photocatalytic performance under 1 sun illumination, demonstrating p-n based type-II heterojunction [117]. Also, a ternary heterostructure of 1D $TiO_2$/CdS/ZnS was developed that showed highest photocurrent density of 5.84 mA/$cm^2$ and photovoltaic efficiency of 3.43 % due to formation of type-II heterojunction. The photoexcited electrons travel from CB of ZnS to CdS to $TiO_2$ for reduction and holes in their VB travel in opposite direction. The passivation of ZnS layer possess a low mismatch quantum dot (QDs) and CB is more negative inhibit electrons to enter in electrolyte and passivates dangling bond on CdS surface which reduces recombination of CB of CdS and $TiO_2$ [118]. Similarly, $TiO_2$/PbS/ZnS heterojunction was synthesized which worked in the same way, as a ternary heterojunction, as discussed above to increase photovoltaic efficiency 0.20 % [119]. As the charge transfer in type-II heterojunction takes place from CB of one semiconductor to CB of other semiconductor will reduce the spatial electrons and holes transfer due to electrostatic repulsion between electrons and holes. Similarly, the attraction between electrons and holes also hinders the electron from one semiconductor to another. It is finally summed up that it fails to separate the photogenerated electrons and holes and weakens the redox ability.

### 3.2. Direct Z-scheme heterojunction

A heterostructure of $Bi_2S_3$ nanosheets on hydrogen treated $TiO_2$ nanorods (NRs) was developed by facile solvothermal method. The photocurrent density of heterostructure was 2.35 mA/$cm^2$ at 1.23 V vs. RHE that is 16 times higher than bare $TiO_2$NRs. The charge transfer mechanism was investigated via photoluminescence (PL) spectra by using terephthalic acid (TA) as a probe molecule to characterize radical OH production under illumination. In TA solution TAOH with PL emission was centered at 425 nm formed by combining OH with TA. The production of OH radical is more in heterojunction than H-$TiO_2$ and proposed the z-scheme mechanism in heterostructure. The photoanode is exposed under solar light irradiation, the electrons in their valence band migrate to their conduction band leaving the holes behind. As the Fermi-level of both semiconductors exhibit equilibrium the z scheme heterojunction is formed. The electrons of H-$TiO_2$ combine with the holes in the VB of $Bi_2S_3$ which improves the separation and extraction of charge carriers. Meanwhile oxygen vacancies are formed in H-$TiO_2$ due to $H_2$ treatment reducing the charge recombination. The electrons in CB of $Bi_2S_3$ take part in reduction to produce $H_2$ and holes in VB of H-$TiO_2$ cause oxidation of sulfur ion and sulfite ion to sulfate ions [120].

Another photoanode consisting of CdS over $TiO_2$ nanosheets based heterostructure was developed by successive ionic layer adsorption and reaction (SILAR) technique produces photocatalytic $H_2$ of 51.4 μmol/h. The photocatalytic activity is enhanced by Z-scheme heterojunction that causes efficient charge separation and migration of charge carriers from $TiO_2$ nanosheets to CdS nanoparticles at their interface. It is confirmed by PL spectra by using coumarin as a probe molecule. The electrons in the CB of CdS are transferred to $TiO_2$ and Fermi-levels come in equilibrium. During this process an internal magnetic field is produced which restrains transfer of electrons from CdS to $TiO_2$. Therefore, electrons started migrating from CB of $TiO_2$ to VB of CdS and electrons of CdS and holes of $TiO_2$ cause reduction and oxidation at the respective surface active sites [121]. Also, a 2D photoanode of ZnS ($E_g$=3.6 eV) on ZnO ($E_g$=3.2 eV) was synthesized by hydrothermal method indicating the direct z-scheme heterojunction. The mechanism for 2D-ZnS@ZnO represents that the CB potential and VB potential of ZnS are −0.31 eV and 2.89 eV. The CB edge potential and VB edge potential of ZnO are 2.56 eV and −0.14 eV. As the CB of ZnO is not more negative than the reduction potential for the photocatalytic hydrogen production. Therefore, it can possibly form the Z scheme heterojunction for photocatalytic hydrogen generation. Upon solar light illumination, the electrons of ZnO and ZnS stimulated from VB to the CB leaving the holes in the VB. The photogenerated electrons are accelerated by built-in electric field in the ZnO and formation of electrostatic attraction at the interface of the heterostructure. The least effective electrons of ZnO recombine with the holes of ZnS due to electrostatic attraction between electrons and holes of ZnO and ZnS. The powerful electrons of ZnS react with H+ ions and produce hydrogen and holes are scavenged by electrolyte. The direct Z scheme nanocomposite of 2D-ZnS@ZnO produces photocatalytic hydrogen is 1552 μmol [122]. Similarly, a direct Z scheme heterojunction of $WO_3$ and ZnS was developed for degradation of tetracycline antibiotic 48.8 % by hydrothermal method. The mechanism involves recombination of photogenerated electrons of ZnS CB and holes of $WO_3$ VB which supports role of $O_2$ radicals as the potential level of electrons in the CB of $WO_3$ is unable to reduce oxygen. Therefore, electrons and holes of higher reduction and oxidation potential are participating in degradation [123] as shown in Fig. 11. Also, a direct Z- scheme core-shell hybrid nanofiber of $TiO_2$/NiS was synthesized by hydrothermal and electrospinning methods. The heterostructure produced 655 μmol/g/h hydrogen from water not from H-containing contaminants. The scheme shows recombination of electrons of $TiO_2$ and holes of NiS while electrons of NiS shows reduction of water and holes of $TiO_2$ shows oxidation of sacrificial agent of methanol [124]. Furthermore, a Z-scheme heterojunction of CdS/$BiVO_4$ composite with 15–20 nm thickness produces more $CH_4$ and CO than the composite with 55–75 nm thickness of $BiVO_4$ nanosheets. The difference in their activities is due to more visible light irradiation, small electron diffusion length, less charge recombination, more charge separation and formation of Z scheme heterojunction. The production of $CH_4$ and CO by nanosheet of $BiVO_4$ is 8.73 and 1.95 μmol $g^{-1}$ after 5 h irradiation [125]. The direct Z scheme heterojunction has many advantages due to formation of heterojunction without any mediator. Firstly, the temporal stability of this heterojunction is considerably prolonged because of resistance to photocorrosion which usually occurs due to the presence of solid mediators. Secondly, the backward reactions in the photocatalysts are weakened. Thirdly, the shielding effect of solid mediators between the charge carriers between both semiconductor photocatalysts reduces. Finally, the binary structure is favorable over the ternary structure which is comparable to type-II heterojunction due to facile and cost-effective fabrication.

### 3.3. Solid-state Z-scheme heterojunction

Xu et. al., prepared a ternary composite of CdS/Ag/$TiO_2$ NTs by

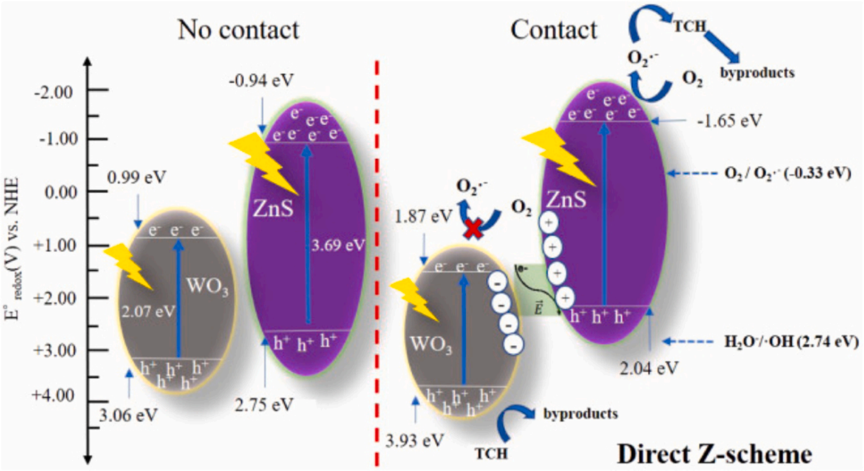

**Fig. 11.** Schematic representation of charge transfer for ZnS /$WO_3$ nanocomposite for Tetracycline Degradation. Reproduced with permission [123]. Copyright 2021, Elsevier.

hydrothermal, photoreduction and SILAR method to increase photocatalytic activities (Fig. 12a-c). The composite showed photodegradation of RhB 82.24 %/3 h and MB 100 %/2 h (Fig. 12c) and rate of $H_2$ production is 806.33 μmol/h/$cm^2$ in one hour. The increase in photocatalytic activities is due to the synergetic effect between $TiO_2$, Ag and CdS showing an indirect Z scheme. The band gap of $TiO_2$ NTs is 3.15 eV with CB and VB values are −0.26 eV and 2.89 eV and the band gap of CdS is 2.16 eV with CB and VB values are −0.40 eV and 1.76 eV. Under light illumination, photoexcited electrons in CB of CdS and holes in the VB of $TiO_2$ recombine on Ag surface. Meanwhile electrons in CB of $TiO_2$ and holes in the VB of CdS cause formation of $O_2^-$ and OH radicals further involved in photodegradation and $H_2$ production (Fig. 12a) [126].

Noticeably, an indirect Z-scheme heterojunction of $TiO_2$-Au-CdS showed photocurrent density of 6.99 mA/$cm^2$ at 1.23 V vs. RHE that is 1.89 times higher than $TiO_2$-CdS and $H_2$ production is 46.64 μmol/$cm^2$/h that is 84.50 times higher than pristine $TiO_2$ due to Au bridge. Under light illumination, photoelectrons migrated to their CB. The electrons of $TiO_2$ transferred to Au nanoparticles through the Schottky barrier and holes of CdS to Au and recombination occurs. The electrons of CdS migrated to CB of $TiO_2$ causes reduction of water while holes of $TiO_2$ transfer to VB of CdS and quenched by sulfide ions of electrolyte [127]. Also, 3D $TiO_2$-Au-CdS produced 1.81 mmol/h/g by above mentioned mechanism [128]. Similarly, a solid-state Z-scheme of ZnO-Au@CdS was prepared which has 79 and 28 times higher photocatalytic activity than ZnO and ZnO-Au [129]. Also, a 3D heterostructure of CdS-Au-ZnO was developed by hydrothermal, sonication and seeding which produced photocatalytic hydrogen of 102.9 μmol/h. Under light illumination, electrons of CdS and ZnO got excited and migrated to their CB. Au acts as electron mediator and produces surface plasmon effect resonance (SPR) effect. The electrons after band alignment transfer from CB of ZnO to Au and holes of CdS to Au cause recombination and increase the flow of electrons to CB of CdS and increase the reduction of water with higher reduction potential. Meanwhile, holes in VB of ZnO cause oxidation of sacrificial agents in the electrolyte [130]. The discussion of solid-state Z scheme heterojunction presented the key factors for enhancing the catalytic activity of the photoinduced interparticle electron and hole transfer. (a) The rate determining step is the charge transfer from one semiconductor to another via solid mediator. (b) The photoactivity of the photocatalysts is enhanced by the balance of conductivity and hydrophobicity of the mediator. (c) The control of annealing time and temperature reduces the

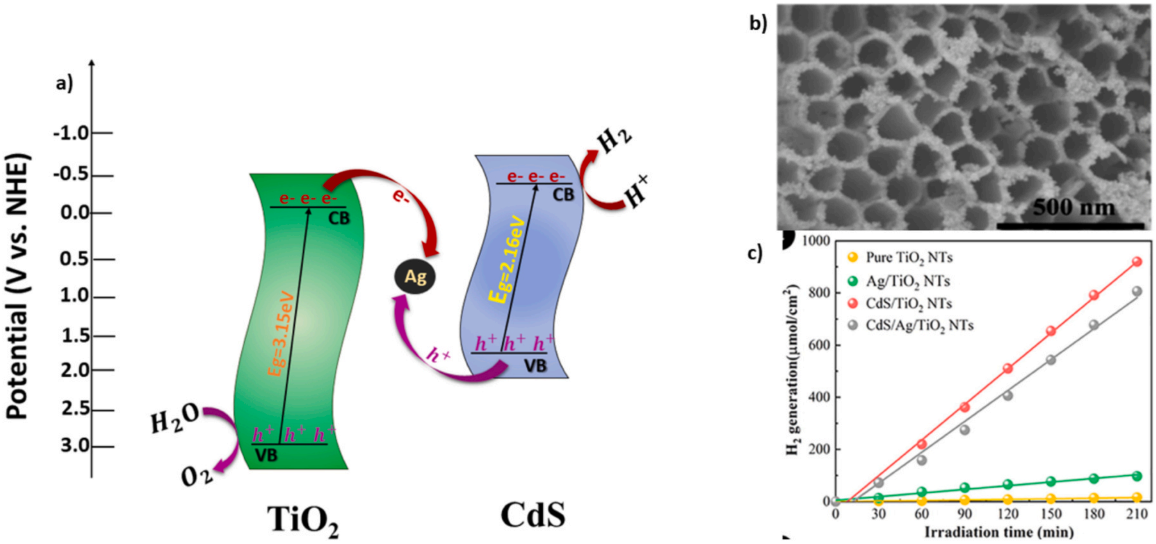

**Fig. 12.** a) Schematic illustration of charge transfer of $TiO_2$/Ag/CdS heterostructure, b) SEM of $TiO_2$/Ag/CdS heterostructure and c) Dye absorbance after photocatalyst adsorption. Reproduced with permission [126]. Copyright 2022, Elsevier.

resistance of charge transfer between the mediator and the semiconductor photocatalyst as well as the Schottky barrier between the metal and semiconductor is also minimized.

### *3.4. S-scheme heterojunction*

For the photocatalytic reaction S scheme heterojunction plays an important role to enhance the photoactivity. There are some strategies to develop the S scheme heterojunction photocatalysts with stronger redox ability such as; Cocatalyst loading, morphology control, interface optimization and reaction activation barrier for charge carrier transfer. For example; Park et. al., synthesized a core-shell CoS@$TiO_2$ heterostructure by positively charged cobalt sulfide micro sheet particles and negatively charged $TiO_2$ nanoparticles using hydrothermal method (Fig. 13a-c). The setup for $H_2$ production and determination was developed (Fig. 13a). The CoS@$TiO_2$ photoanode has strong ability to absorb visible light and produced 1945 μmol/g for 10 h (Fig. 13b) which is 114.4 and 13.2 times higher than p-CoS (E=1.57 eV) and n-TiO2. Generally, as the intensity of PL spectra decreases the recombination of electrons and holes decreases and photocatalytic performances increase. In CoS@$TiO_2$ heterojunction very low intensity of PL spectra is obtained at 825 nm so the electrons in CoS particles did not relax through interface transitions after excitation from S 2p to Co 3d and remained in the core shell. Therefore, electrons did not flow from CoS to $TiO_2$ nanoparticles and followed the S-scheme mechanism (Fig. 13c). This mechanism consists of reduction photocatalyst (RP) and oxidation photocatalyst (OP) with staggered band gap energies equal to energy of z-scheme. But in s-scheme redox potential is way stronger than z-scheme due to recombination of unnecessary electron-hole pairs. According to spin-coating ESR trapping mechanism, under solar light OH radicals gather in VB of $TiO_2$ and $O_2^-$ radicals gather in CB of CoS and show an s-scheme mechanism instead of type-II. In this scheme electrons get excited under light illumination in both photocatalysts and migrate to CB. The electrons travel from CB of CoS to VB of $TiO_2$ while electrons of $TiO_2$ cause reduction of water and holes of CoS cause oxidation of lactic acid [131].

Noticeably, a ternary p-n-p heterojunction- based S-scheme containing CuO/CdS/$CoWO_4$ was developed by hydrothermal and microwave hydrothermal methods. The photoanode showed higher values of catalytic hydrogen production which is 457.9 $\mu molg^{-1}h^{-1}$ that is 3.14, 11.99, 40.88 and 102.9 times higher than CuO/CdS, CdS, CuO and $CoWO_4$, respectively. The band gap of the photoanode is 2.40 eV. This heterojunction shows stability even after five cycles during production of $H_2$ and can be reused. After in contact, an internal electric field is produced causing adjustment of their Fermi-levels and electrons are migrated from CB of CuO and CB of $CoWO_4$ to VB of CdS. The electrons of CdS cause reduction and holes of CuO and $CoWO_4$ cause oxidation [132]. Chen et. al., developed an S-scheme based CuO/CdS QDs for degradation of chlortetracycline up to 86.8 % and have current density 3.42 $A/m^2$. The PL spectra show excitation wavelength at 350 nm to avoid charge carrier recombination. Electrons of CuO and holes of CdS combine and electrons of CdS and holes of CuO cause reduction and oxidation [133]. Also, S-scheme heterojunction in $TiO_2$/CdS nanocomposite produces photocatalytic hydrogen of 2.32 mmol/h/g which is 35 times higher than the pristine $TiO_2$. The electrons of $TiO_2$ are useless and recombine with holes of CdS. Meanwhile the useful electrons of CdS cause reduction of water and holes are quenched by methanol [134]. Similarly, a S-scheme heterojunction of CdS/$TiO_2$ hollow microsphere was prepared by hydrothermal method for reduction of $CO_2$ to $CH_4$. The photocatalytic reduction produces 27.85 μmol $g^{-1}$ $h^{-1}$ which is 145.6 and 3.8 times higher than pristine CdS and $TiO_2$ due to multi scattering of visible light, photocatalytic reactions take place on both outside and inside surface of shell and intimate contact between both semiconductors making S scheme by in-built electric field causing reaction at higher redox potential [135].

Among the discussed examples of metal oxide and metal sulfide composites, $TiO_2/Sb_2S_3$ has highest photocurrent density 9.0 $mA/cm^2$ at 1.23 V vs. RHE due to placing Pt co-catalyst and buffering layer $In_2S_3$ in between $TiO_2$ and $Sb_2S_3$. It is prepared by atomic layer deposition and chemical bath deposition having charge transfer mechanism is of type-II heterojunction. But $TiO_2$-Au-CdS has 6.99 $mA/cm^2$ photocurrent density at 1.23 V vs. RHE under 1 sun illumination. It has Au metal as a bridge due to very low concentration producing Schottky barrier and increases the flow of electrons to CB of $TiO_2$ for $H_2$ production and reduces the recombination of charges creating indirect Z-scheme heterojunction. $TiO_2$ NTs-Ag-CdS composite prepared by hydrothermal, electrospinning and SILAR methods gives highest value of degradation of organic dyes (MB and Rh B) 100 %, 82 % and produce $H_2$ 806.33 μmol/g/h due least electron recombination and SPR effect of Au. At the end there are few points which are necessary to choose the photocatalysts for best heterojunction to enhance the activity of that composite. These are: appropriate matching of CB and VB potential, stability of the composite in the electrolyte, highly stable in the light, effective charge separation, beneficial charge transfer which leads to water

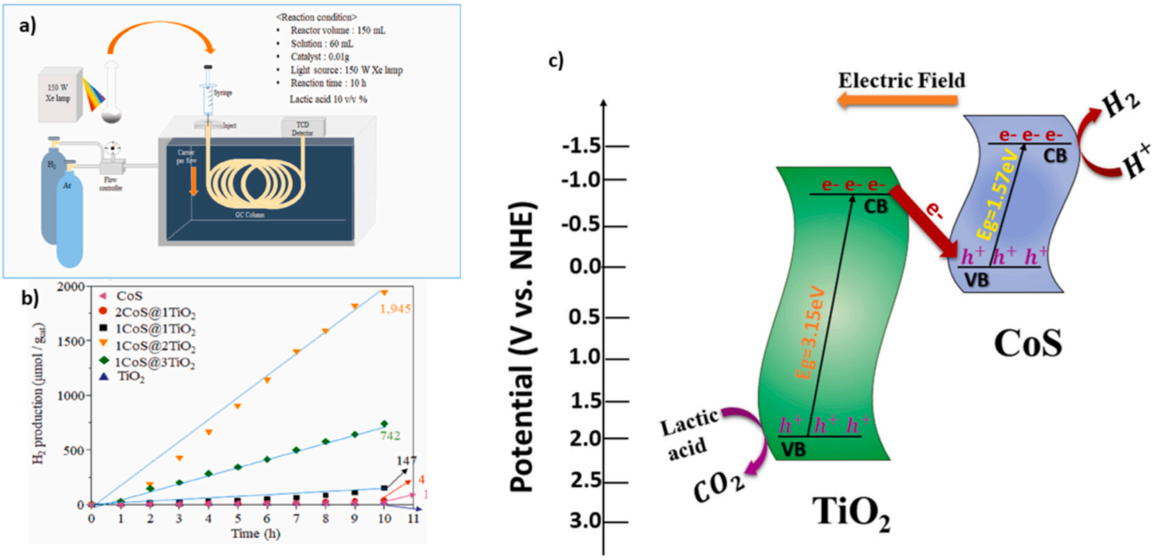

**Fig. 13.** a) Schematic diagram for CoS@$TiO_2$ core-shell heterojunction b) $H_2$ production from water splitting in the presence of lactic acid. Reproduced with permission [131]. Copyright 2021, Elsevier.

splitting and reduction of $CO_2$ at better redox potentials and degradation of dyes to less harmful material. The best heterojunction of metal oxide and metal sulfide photocatalysts can be formed by selection of metal oxide and metal sulfide which overcome the weakness of each other. For example, metal oxides possess poor separation efficiency, low mobility, slow surface gas evolution efficiency. Therefore, metal sulfide should be selected which have narrow band gap, high light absorption efficiency to facilitate charge separation, transfer and subsequently, promote respective product formation and desorption kinetics from the surface active sites. By keeping all these aspects, an accountable scheme containing ternary nanocomposite is introduced as shown in Fig. 14 which could be helpful to enhance the activity of any heterojunctions based upon metal oxide-metal sulfide heterojunctions schemes for different kind of reactions such as $CO_2$ reduction, water reduction, dye degradation and any kind of oxidation reactions. In this scheme of Fig. 14, there are three layers comprised as: semiconductor-1, semiconductor-2 and semiconductor-3 with band gap of first layer may be greater than or equal to 2.0 eV, second layer may have band gap greater than or equal to zero and less than or equal to 2 eV and third layer may have band gap equal to or greater than 2.5 eV. The semiconductor-1 catalyst might be CB lower than zero potential so its electrons cannot be able to do effective reduction and semiconductor-2 has CB band higher than zero potential but VB is higher than oxidation potential required for any kind of oxidation reaction. Meanwhile semiconductor-3 can have CB at higher reduction and higher oxidation potential and higher stability but wide band gap which may not be feasible for any reaction to occur. After knowing the pros and cons of every layer a heterojunction can be formed that may have maximum electrons to participate in the reduction reaction and maximum holes for oxidation reactions. Under light illumination the electrons absorb visible light and migrate from VB to CB. Due to migration of charge carriers an internal field is produced which creates an interface between all three-semiconductor catalysts. According to type of interface between semiconductor-1 and semiconductor-2 useless electrons of first layer can recombine with holes of second layer. Meanwhile the electrons from CB of third layer may transfer to CB of second layer due to different type of interface formation and these electrons can cause reduction reaction. The holes of semiconductor-2 might be used up for recombination; the holes from VB of semiconductor-1 may migrate to VB of semiconductor-3 because holes always travel from more positive VB to less positive VB and cause oxidation reactions. Let's explain this scheme by taking an example of ternary nanocomposite consisting of metal oxide and metal sulfide layers and can be represented as: semiconductor-1 and semiconductor-3 can be MO-1 and MO-3 and semiconductor-2 is considered as MS-2 layers. The percentage composition of every layer could be adjusted according to requirements for the reaction to proceed with high photocatalytic activity. Here, MO-1 layer can be 20 % because no reaction can take place on this layer but its band gap is small so it might help in absorption of maximum visible light. MS-2 layer might be 50 % because maximum reactions like water splitting, $CO_2$ reduction to aldehyde, methane, CO, alcohol and dye degradation could take place. Meanwhile the composition percentage of MO-3 layer may be 30 % because it has wide a band gap which can be helpful to provide stability to heterostructure and also transfer electrons to CB of MS-2 which cause reduction reaction and can take holes from MO-1 to its VB to do oxidation reaction. Lastly, this scheme can be used for any kind of ternary composite like metal sulfides, metal oxides, metal carbides, metal nitrides and many more and can also be utilized for more than two reactions at a time.

## 4. Metal sulfide-metal sulfide composites

Metal sulfides are introduced as a good candidate for visible light driven reactions such as photoelectrochemical water splitting to produce $H_2$ and $CO_2$ reduction. Remarkably, metal sulfides have better electron/hole pair separation efficiency than metal oxides, therefore, they are used as better visible light driven photocatalysts [138]. The valence band of metal sulfides are occupied by S-3p orbitals, and their position is higher than O-3p orbitals, which gives rise to form less positive VB and higher mobility of electrons and holes for acceleration of charge transfer in them. Metal sulfides have unique features like suitable band gap, tunable surface electronic configuration, and abundant active sites for water splitting applications to produce hydrogen [139]. Metal sulfides have a problem of photo corrosion which can be solved by forming composites with other somewhat stable metal sulfides.

### 4.1. Type-II heterojunction

Type-II of $MnIn_2S_4/Cu_7S_7$ heterojunction has improved hydrogen production activity which is 13.81 μmol/h (Fig. 15a-b) that is 18 times higher than pristine $MnIn_2S_4$. It is due to p-n heterojunction which exhibits inhibition of charge recombination and higher charge carrier separation (Fig. 15a). In this heterojunction, CB values of $MnIn_2S_4$ and $Cu_7S_4$ are −0.61 V and −0.99 V and Fermi-level of $MnIn_2S_4$ is below its CB and Fermi-level of $Cu_7S_4$ is above its VB. When the light falls on the composite the electrons in the valence band of both semiconductors get

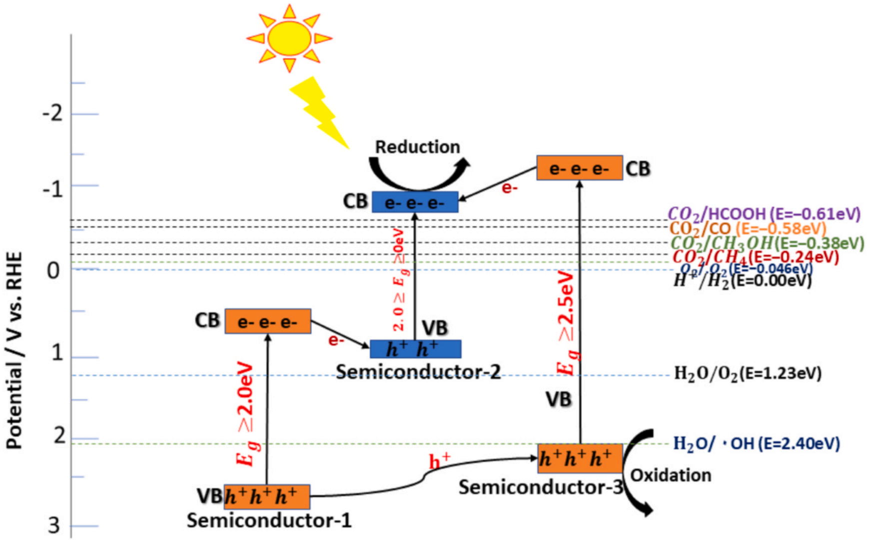

**Fig. 14.** Scheme for semiconductors with different band alignments for transfer of charger carriers.

**Table 2**
Metal oxide-metal sulfide-based heterojunctions for Photocatalytic applications:.

| Photocatalysts-Sensitizers | Synthesis Methods | Heterojunction | Activities | References |
|---|---|---|---|---|
| $AgFeO_2$-$ZnIn_2S_4$ | Coprecipitation-Solvothermal | Type-II | 0.006 (mA/$cm^2$) Photocurrent Density at 1.23 V vs. RHE | [111] |
| $TiO_2$ NRs-$CdIn_2S_4$ | Hydrothermal-Hydrothermal | Type-II | 3.8 (mA/$cm^2$) Photocurrent Density at 1.23 V vs. RHE | [112] |
| $TiO_2$ NRs-$ZnIn_2S_4$ | Hydrothermal-Hydrothermal | Type-II | 1.2 (mA/$cm^2$) Photocurrent Density at 1.5 V vs. RHE | [113] |
| 3D rosette $TiO_2$ NRs-$Bi_2S_3$ | Hydrothermal-SILAR | Type-II | 3.98(mA/$cm^2$) Photocurrent Density at 1.23 V vs. RHE | [114] |
| $TiO_2$-$Sb_2S_3$ | ALD-CBD | Type-II | 9.0 (mA/$cm^2$) Photocurrent Density at 1.23 V vs. RHE | [115] |
| $TiO_2$-$In_2S_3$ | Hydrothermal-Spin Coating | Type-II | 0.1256 (mA/$cm^2$) Photocurrent Density at 1.23 V vs. RHE | [116] |
| α-$Fe_2O_3$-$Bi_2S_3$ | Hydrothermal-SILAR & Solvothermal | Type-II | 2.550 (mA/$cm^2$) Photocurrent Density at 1.23 V vs. RHE | [117] |
| $TiO_2$-CdS-ZnS | Hydrothermal-SILAR-SILAR | Type-II | 5.84 (mA/$cm^2$) Photocurrent Density at −1.23 V vs. RHE and photovoltaic efficiency 3.43 % | [118] |
| TiO2-PbS-ZnS | Hydrothermal-SILAR-SILAR | Type-II | Photovoltaic efficiency 0.20 % | [119] |
| H-$TiO_2$ NRs-$Bi_2S_3$ | Hydrothermal-Solvothermal | Direct Z-scheme | 2.35 (mA/$cm^2$) Photocurrent Density at 1.23 V vs. RHE | [120] |
| $TiO_2$ nanosheets-CdS nanoparticles | SILAR-SILAR | Direct Z-scheme | 0.15 (mA/$cm^2$) Photocurrent Density Vs. RHE | [121] |
| ZnO-ZnS | Hydrothermal-Hydrothermal | Direct Z-scheme | 0.72 (mA/$cm^2$) Photocurrent Density and 1552 μmol $H_2$ | [122] |
| $WO_3$-ZnS | Hydrothermal-Hydrothermal | Direct Z-scheme | Degradation of Tetracycline antibiotic is 48.8 % | [123] |
| $TiO_2$-NiS | Hydrothermal-Spin Coating | Direct Z-scheme | Production of $H_2$ is 655μmol/g/h | [124] |
| $BiVO_4$-CdS | Hydrothermal-CBD | Direct Z-scheme | Production of $CH_4$ and CO is 8.93 and 1.95μmol $g^{-1}$ by reduction of $CO_2$ | [125] |
| $Cu_3BiS_3$-$MoS_2$ | Hydrothermal | Direct Z-scheme | Production of $H_2O_2$ 1457 μM $h^{-1}$ | [136] |
| $TiO_2$-Au-CdS | Hydrothermal-Electrodeposition-SILAR | Solid-state Z-scheme | 6.99 (mA/$cm^2$) photocurrent density at 1.23 V vs. RHE | [127] |
| $TiO_2$ NTs-Ag-CdS | Hydrothermal-Electrospinning-SILAR | Solid-state Z-scheme | Degradation of Rh B and MB is 82.24 % and 100 %. $H_2$ production is 806.33μmol/g/h | [126] |
| CdS-Au-ZnO | Hydrothermal-Sonication-Spin coating | Solid-state Z-scheme | Photocatalytic production of $H_2$ is 102.9 μmol/h | [130] |
| $TiO_2$-CoS | Hydrothermal-Hydrothermal | S-scheme | 0.012 (mA/$cm^2$) Photocurrent Density at 1.23 V vs. NHE | [131] |
| CuO-CdS-$CoWO_4$ | Hydrothermal-Microwave hydrothermal -Microwave hydrothermal | Double S-scheme | Photocatalytic production of $H_2$ is 457.9 μmol/h/g | [132] |
| CuO-CdS | SILAR-Hydrothermal | S-scheme | Degradation of chlortetracycline is 86.6 % | [133] |
| $TiO_2$-CdS | Electrospinning-Electrospinning | S-scheme | Photocatalytic production of $H_2$ is 2320μmol/g/h | [134] |
| CdS-$TiO_2$ | Hydrothermal-Hydrothermal | S-scheme | Photocatalytic reduction of $CO_2$ to $CH_4$ is 27.85μmol $g^{-1}$ $h^{-1}$ | [135] |
| $SnNb_2O_6$/CdS | In-situ microwave solvothermal method | S-scheme | Photocatalytic production of $H_2O_2$ is 7808 μmol $g^{-1}$ $h^{-1}$ | [137] |

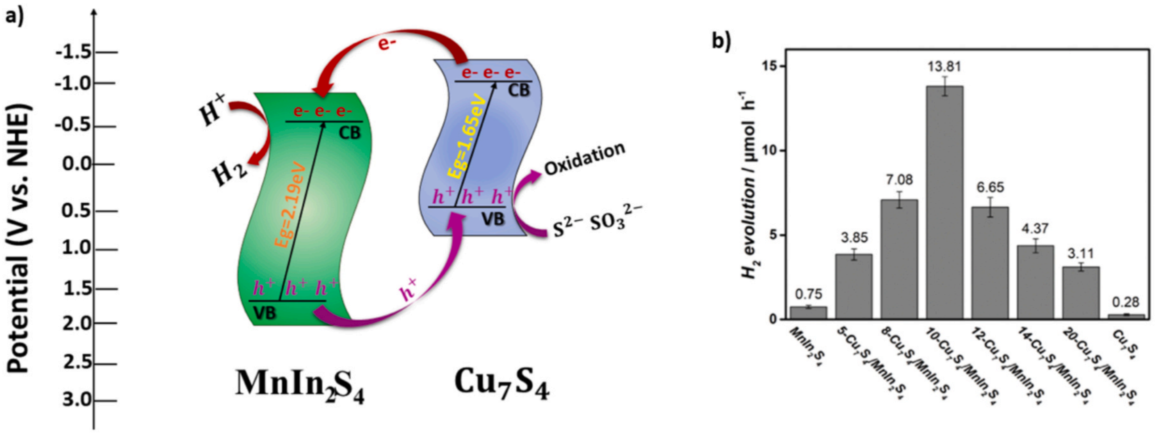

**Fig. 15. a) Schematic illustration of the possible mechanism for the photocatalytic $H_2$** production of **$Cu_7S_4/MnInS_4$** b) Hydrogen production of **$Cu_7S_4$**/$MnIn_2S_4$ heterostructure. Reproduced with permission [140]. Copyright 2021, Elsevier.

excited and migrate to their conduction bands leaving holes behind. Due to light irradiation and charge carriers' interface is formed between both semiconductors and Fermi-levels of both semiconductors come in equilibrium due to internal electric field. Then, the electrons would migrate from CB of $Cu_7S_4$ to CB of $MnIn_2S_4$ and holes travel in opposite directions in their VB. It leads to separation of electron-hole pairs and inhibits the recombination of charge carriers. In this heterojunction, $MnIn_2S_4$ acts as n-type semiconductor and $Cu_7S_4$ is p-type semiconductor and electrons travel from p-type to n-type as a result p-n heterojunction (Fig. 15a) is formed. As electrons migrate from CB of $Cu_7S_4$ to CB of $MnIn_2S_4$ and holes in opposite directions, indicating Type-II mechanism [140].

Similarly, $Bi_2S_3$/CdS heterostructure was developed by facile and one-step sono-chemical methods. The photocatalytic hydrogen produced by composite (CdS/$Bi_2S_3$, x=0.15) is 5500 μmol/g/h which is much higher than bare CdS photocatalyst (40 μmol/g/h). The enhancement in production of photocatalytic hydrogen is because of adjustment of bands for higher charge transfer and lower charge recombination. The charge transfer type-II mechanism is investigated by PL spectra as higher the PL intensity more the effective charge carriers participate in recombination while lower the PL intensity more the effective charge separation in the composite which increase the photocatalytic activities. Photoexcited electrons migrated from CB of CdS to $Bi_2S_3$ and holes in opposite direction and cause reduction and oxidation [141]. Also, dense array of CdS-ZnS core-shell nanorod film was established by aerosol assisted chemical vapor deposition (AACVD) method. The formation of ZnS nanocrystal on CdS nanosheets restrain photo-corrosion, enhance photoelectrochemical activities such as; increased charge separation and transportation efficiencies. The photocurrent density of heterostructure is 7.8 mA/$cm^2$ and IPCE value is above 35 % under AM1.5 G one sun illumination. The enhancement in photocurrent density and IPCE exhibited a spatial charge transfer mechanism in the CdS/ZnS nanostructure. Under light illumination, both photogenerated electrons and holes of CdS are difficult to transfer from CdS to ZnS. According to PEC performances, there are other paths for transfer of holes from valence band of CdS band gap=2.4 eV) to VB of ZnS (band gap=3.6 eV). There are different intrinsic defects like sulfur vacancies ($V_s$), zinc vacancies ($V_{Zn}$) and interstitial sulfur ($I_s$) in ZnS. These acceptor states are higher than VB of ZnS and help to transfer holes from VB of CdS to VB of ZnS. The enhancement in the photocurrent density is due to migration of holes from CdS to ZnS by passing from these acceptor sites. Under light illumination, electrons get excited in VB of both semiconductors and migrate from VB to CB. Finally, electrons reach the Pt electrode by passing from CB of ZnS to CB of CdS and cause reduction of water. While holes transfer in opposite directions and exhibit quasi type-II (Fig. 16a) heterojunction [142]. While CdS-ZnS core-shell heterostructure was developed that has produced 830.95 μmol/g/h (Fig. 16b) photocatalytic hydrogen by forming quasi type-II heterojunction [143]. Also, hierarchical $In_2S_3$-$CdIn_2S_4$ nanostructured nanotubes prepared by cation exchange reaction and hydrothermal cation exchange reaction with 5 minutes and 10 minutes reaction time to adjust the morphology of final product and form different composites as $In_2S_3$-$CdIn_2S_4$-5 and $In_2S_3$-$CdIn_2S_4$-10. The $In_2S_3$-$CdIn_2S_4$-10 showed highest production of CO from $CO_2$ is 825 μmol $h^{-1}$ $g^{-1}$. It is due to higher separation of charge carriers, higher values of transfer kinetics of photoexcited charge carriers and these factors are attributed to unique composition and hierarchical structure of this nanotube [144]. The type-II heterojunction in the metal sulfide-metal sulfide based composites offers the enhanced photocatalytic activity due to enhanced charge carrier separation and broad visible light absorption spectra but it has some challenges which are complex synthesis process, internal defects at the interface of the semiconductors, high cost, scalability and stability which make them less effective for the photocatalytic application.

### 4.2. Direct Z-scheme heterojunction

Direct Z-scheme based heterojunction of CdS@$ZnIn_2S_4$ hollow cubes photoanode was prepared by low-temperature solvothermal method. The photocatalytic hydrogen production of heterostructure is 540.3 μmol/gh which is three times higher than $ZnIn_2S_4$ nanosheets (0.2μmol/gh). According to Mott-Schottky plot, the band gap energy value of n-type $ZnIn_2S_4$ is 2.53 eV with CB and VB values are −0.57 V and 1.96 V. The band gap energy value of n-type CdS is 2.21 eV with CB and VB values are −0.90 V and 1.31 V. These band alignments of CdS and $ZnIn_2S_4$ results in increasing the possibilities of Z-scheme mechanism based photoexcited charge transportation. DFT calculations (Fig. 17a) show that band bending CdS-$ZnIn_2S_4$ interface is formed as the work function of CdS (103) was estimated 4.92 eV and 4.21 eV smaller than $ZnIn_2S_4$ (104) surface at 5.20 eV. EPR spectrum indicated successful detection of OH species further authenticated the Z scheme formation. Surface photovoltage mapping image (SPV) shows that composite has more positive signals than single composite and composite induced vectorial charge transfer from $ZnIn_2S_4$ to CdS and Z scheme pathway was depicted. Therefore, electrons are migrated from CdS surface having higher Fermi-level to $ZnIn_2S_4$ surface having lower Fermi-level to equilibrate Fermi-levels of both semiconductors. After Fermi-level equilibrium there is the appearance of electron layer depletion (Fig. 17b) in CdS and charge density difference in $ZnIn_2S_4$ producing internal electric field. It may allow recombination of electrons of $ZnIn_2S_4$ and holes of CdS following the Z-scheme mechanism (Fig. 17c). The electrons of CdS and holes of $ZnIn_2S_4$ cause reduction and oxidation of water to produce hydrogen and $H_2O_2$ [145].

Direct Z-scheme flower-like $Bi_2S_3$/$SnIn_4S_8$ heterojunction was synthesized for degradation of Rhodamine B which is 99.87 %. Schottky barrier is formed by combination of electrons of $Bi_2S_3$ and holes of $SnIn_4S_8$ ($E_g$ =1.77–2.35 eV), while electrons of $SnIn_4S_8$ cause degradation [146]. The hollow $MoSe_2$@$Bi_2S_3$/CdS core-shell structure was established and demonstrated dual Z-scheme heterojunction which increases the rate of quantum conversion efficiency, interface area and active sites. The ternary structure showed excellent photocatalytic activities like $H_2$ production 11.84 mmol/g/h, removal of Cr (VI) 98.7 % and 2,4,6-trichlorophenol (TCP) 99.2 %. Electrons of $Bi_2S_3$ and CdS recombine with holes of $MoSe_2$ while electrons of $MoSe_2$ cause reduction of water, Cr(IV) and $O_2$ [147]. It is concluded that the synthesis methods play an important role to synthesize spatial type of heterojunction. Therefore, to synthesize the direct Z scheme heterojunction can be the deposition-precipitation methods, hydrothermal and solvothermal methods. Similarly, the best characterization techniques can be the DFT calculations, EPR analysis, SPVM and in-situ XPS.

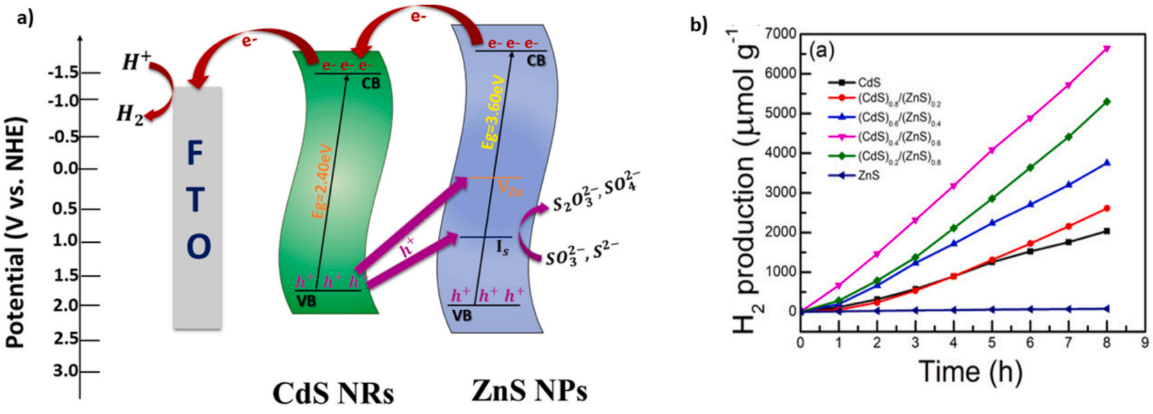

**Fig. 16.** a) Schematic representation of charge generation and transfer in CdS/ZnS heterojunction b) Photocatalytic $H_2$ production in CdS-ZnS composite with different concentrations. Reproduced with permission [143]. Copyright 2019, American Chemical Society.

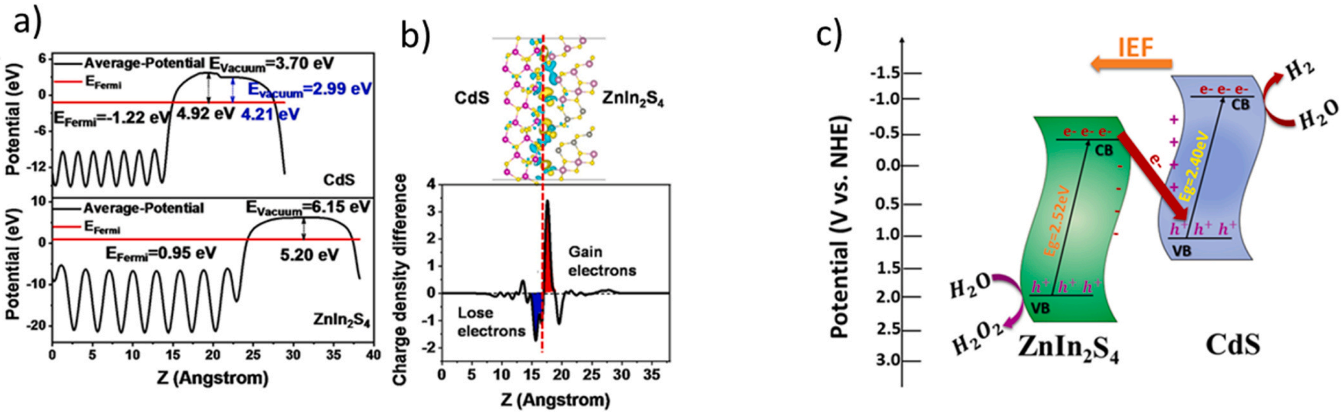

**Fig. 17.** a) Electrostatic Potential for CdS (103) surface and $ZnIn_2S_4$ (104) surface b) Simulated charge distribution at interface to get Fermi-level at equilibrium c) Charge transfer mechanism in Z-scheme heterojunction. Reproduced with permission [145]. Copyright 2021, Elsevier.

### 4.3. Solid-state Z-scheme heterojunction

A solid-state Z-scheme heterojunction was demonstrated by using ternary $CdS/MoS_2$ QDS/$ZnIn_2S_4$ heterojunction, where $MoS_2$ QDs acts as electron mediator. The ternary photocatalyst produces hydrogen of 2107.5 μmol/g/h which is 26 and 62 times higher than CdS NRs and ZIS nanosheets, respectively. The increase in photocatalytic activity is due to the formation of z-scheme (Fig. 18) by insertion of QDs in between CdS and ZIS. The electrons on photoexcitation would travel from CB of CdS to $MoS_2$ QDs to VB of ZIS and then get excited and reach CB of ZIS where reduction occurs. In the same way, holes in VB of CdS cause oxidation of lactic acid and EIS of hybrids also show lower recombination than their bare forms [148]. Similarly, a ternary structure of ZnS/rGO/$Bi_2S_3$ showed switching of heterojunction from type-II to solid-state Z-scheme due to introduction of rGO as an electrons mediator. It converts 18.4 % solar-to-hydrogen conversion efficiency which is 2523.4 μmol/g/h and showed the highest photocurrent density of 38 mA/$cm^2$. The RGO plays an important role in enhancing the production of hydrogen due to large surface area, good conductivity, tunable band gap and hydrophobicity due to C-C bonds [149]. Furthermore, a Z-scheme heterostructure with Cd as metal bridge between $Co_9S_8$ ($E_g$ =1.23 eV) and CdS was also demonstrated to enhance the photocatalytic hydrogen evolution to 10.42 μmol/h which is 5.7 times higher than for pristine Cd/CdS [150].

### 4.4. S-scheme heterojunction

Goh et. al., enhanced photostability and photocatalytic activities of petal-shaped CdS by forming heterojunction with $FeS_2$ nanoparticles. The heterostructure is prepared by thermal treatment methods at different temperatures with photocatalytic hydrogen 107.56 mL/g. For estimation of charge transfer mechanism in CdS/$FeS_2$ heterojunction interface DMPO was used as a trapping agent to detect •OH and $\bullet O_2^-$ and spin trapping analysis was performed. Even after 30 minutes of simulated sun irradiation (Fig. 19a), the DMPO-•$O_2$ signal strength in the $FeS_2$ particles was low. Yet, as it was a little stronger than the DMPO-•OH signal strength, it was determined that the $FeS_2$ particles were the source of the •$O_2$ radicals. Yet, the DMPO-•$O_2$ signal in the CdS particles had a very strong intensity that was comparable to the DMPO-•OH signal. We concluded that the •OH radical was produced in the VB of CdS and the •$O_2$ radical was produced in the CB of $FeS_2$ even though the magnitudes of the two signals in $FeS_2$ were not equal. Moreover, the junction of CdS and $FeS_2$ resulted in a considerable rise in the DMPO-•$O_2$ signal, demonstrating the synergy of the two particles. Yet, comparable to the DMPO-•OH signal, the CdS/$FeS_2$ junction catalyst's DMPO-•$O_2$ signal dramatically increased over time. As a result, it can be inferred that during the photocatalytic •$O_2$ radical process, the electrons generated by CdS in the CdS/$FeS_2$ junction particles moved to $FeS_2$ and accumulated more in the CB of $FeS_2$. Hence, it is expected that more •OH radicals were produced in the VB of CdS during the photoreaction in the CdS/$FeS_2$ junction particles and more •$O_2$ radicals accumulated in the CB of $FeS_2$.Here, S-scheme (Fig. 19b) is followed due to build in electric field by reducing transport distance charge carriers at interface between two charge carriers. The built-in electric field removes useless holes and electrons in VB and CB of heterostructure and increases the separation of useful electrons and holes to produce hydrogen [151]. Also, S-scheme heterostructure was constructed to have core-shell $FeS_2$@$ZnIn_2S_4$ with Pt as cocatalyst by quenching the useless electrons from CB of $ZnIn_2S_4$ and using electrons of $FeS_2$ for hydrogen production. The composite produces $H_2$ of 10,100μmol/g/h which is 47.9 times higher than ZIS and 53.7 times higher than $FeS_2$ [152]. Liu et. al., prepared ZnS/ZIS photocatalyst produces hydrogen of 2912.3μmol/g/h which is 9.0 and 33.6

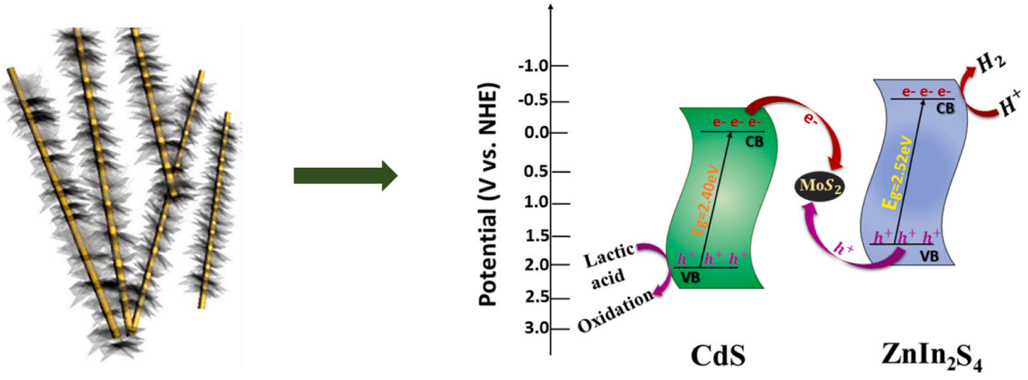

**Fig. 18.** Schematic representation of charge transfer in CdS/$MoS_2$ QDs/$ZnIn_2S_4$ Heterojunction. Reproduced with permission [148]. Copyright 2019, Elsevier.

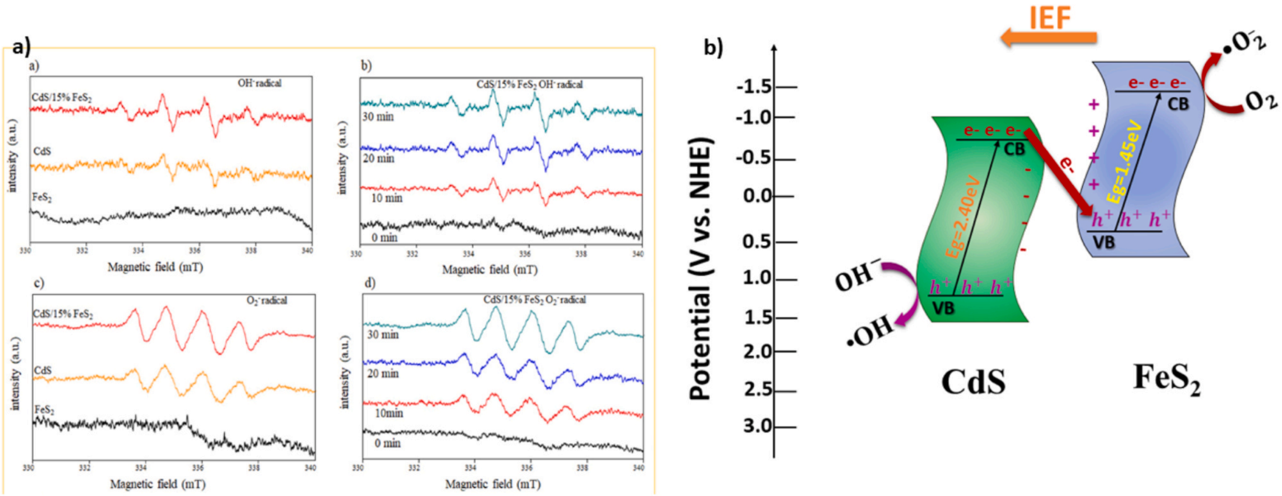

**Fig. 19.** a) DMPO-•O$_2$ signals for CdS/15 % FeS$_2$ under light irradiation b) Charge transfer mechanism on CdS/15 % FeS$_2$ heterojunction. Reproduced with permission [151]. Copyright 2022, Elsevier.

times higher than ZIS and ZnS due to the S-scheme heterojunction formation [153]. Hollow nanostructure of CuS@ZIS was developed and produces enhanced photocatalytic hydrogen of 4653.43μmol/g/h and shows S-scheme heterojunction by energy band structure analysis to increase charge carrier separation [154]. A ternary composite containing CdS nanoparticles and wrapping around RGO sheets onto the surface of $Bi_2S_3$ as template was synthesized and produced $H_2O_2$ 212.82 μmol $L^{-1}$ [155].

From the above discussed examples of all type of heterojunctions of metal sulfide – metal sulfide composite of $MoSe_2$-$Bi_2S_3$-CdS is prepared by solvothermal, and hydrothermal method that produces the highest amount of hydrogen 11840μmol/g/h. The enhancement in photocatalytic activity is due to formation of core-shell structure having huge active sites for excellent light absorption. $Bi_2S_3$ and CdS with $MoS_2$ form dual direct Z-scheme heterojunction and reduce charge recombination by forming multi-channel charge transfer. After the study of metal sulfide and metal sulfide-contained heterostructures it is noted that there are some metal sulfides which may have problems with photo corrosion, poor electrical properties, and poor charge separation. These problems are solved by formation of heterojunction with those metal sulfides and metal oxides which have narrow band gaps are photochemically stable, show great electrical and photocatalytic properties and better charge separation and charge transportation which leads to photocatalysis at lower input energy. To enhance the activity of the heterostructure there is necessary role of selection of type of photocatalyst and their adjustment in such a way that their CB and VB potentials and Fermi-levels matches mutually which further leads to stability to light illumination, charge migration, separation and transportation. According to these factors a scheme is anticipated having three different kinds of layers which might be named as: semiconductor-1, semiconductor-2 and semiconductor-3 with different band alignments to increase the activity to ternary nanocomposite. The band gap of semiconductor-1 may be less than or equal to 3.2 eV, semiconductor-2 may be less than or equal to 2.0 eV and semiconductor-3 may be less than or equal to 2.5 eV. As the CB of all semiconductor photocatalysts might be above zero potential so electrons in their CB can be useful for the reduction reaction. Therefore, such a type of interface can be constructed among all of them so that electrons of all semiconductors can be utilized for the reaction to enhance the activity of the photocatalyst. Under solar light irradiation the charge carriers absorb light and electrons migrate from their VB to CB leaving the holes behind. Due to transportation of charge carriers' interface is formed among all layers. On the basis of interface formation and band positions electrons from CB of semiconductor-1 and semiconductor-3 travel to CB of semiconductor-2 and reduction takes place. Meanwhile, holes from VB of semiconductor-1 transfer to semiconductor-2 and then subsequently to semiconductor-3, where the oxidation reaction takes place. This heterojunction can be illustrated by taking an example as shown in Fig. 20. Let's consider that semiconductor-1 is MO-1 and semiconductor-2 and semiconductor-3 are MS-2 and MS-3. Firstly, percentage composition should be decided that out of 100 %, how much percentage of each layer could be used to develop the efficient nanocomposite based schemes. MO-1 layer can be 25 % because of wide band gap which can make the composite stable and only participate to transfer its charge carriers and MS-2 layer may be of 35 % due to smaller band gap and can absorb maximum visible light and maximum reduction reaction takes place from its CB. Meanwhile, the MS-3 layer may be 40 % with a small band gap which might be helpful to maintain stability, increase light absorption, enhance the charge transportation and take the holes from other two layers to increase the oxidation reaction at its VB (Fig. 20). Lastly, this scheme presented in Fig. 20 would be helpful to enhance the activity of nanocomposite by choosing different materials i.e.; metal-based or non-metal-based semiconductors with adjustable percentage compositions and for different type of redox reactions depending upon the reduction and oxidation potentials of redox species to be utilized for their conversion as shown in Fig. 20.

Among all types of heterojunctions, the Z-scheme mechanism shows the best stability and excellent recyclability. The Z scheme heterojunction mechanisms are made by mimicking the process of natural photosynthesis. In this process, the photogenerated electrons of one semiconductor are recombined with holes of other semiconductor and highly energetic electrons and holes are eventually utilized for redox reactions. Simultaneously, the materials used in the Z scheme heterojunctions have robustness and resistance to photostability and enhance the long-term stability of the photocatalyst. Meanwhile, the S scheme heterojunction might still face issues related to degradation of materials over time. Therefore, Z scheme heterojunction material photocatalysts are preferred on the industrial scale due to their high photostability and recyclability for photocatalytic applications. In contrast, the photostability and recyclability of metal oxides and metal sulfide are also essential for photocatalytic application. The metal oxides such as $TiO_2$, ZnO and $WO_3$ are well known for their excellent resistant to photo corrosion and maintain their structural catalytic behavior under light illumination. They also show stability under high pH levels and temperature. They retain their photocatalytic properties over multiple cycles due to their robust chemical nature and can also be recovered easily. Meanwhile, metal sulfides $Bi_2S_3$ and ZnS are prone to photo corrosion and degrade under continuous light illumination. They are not

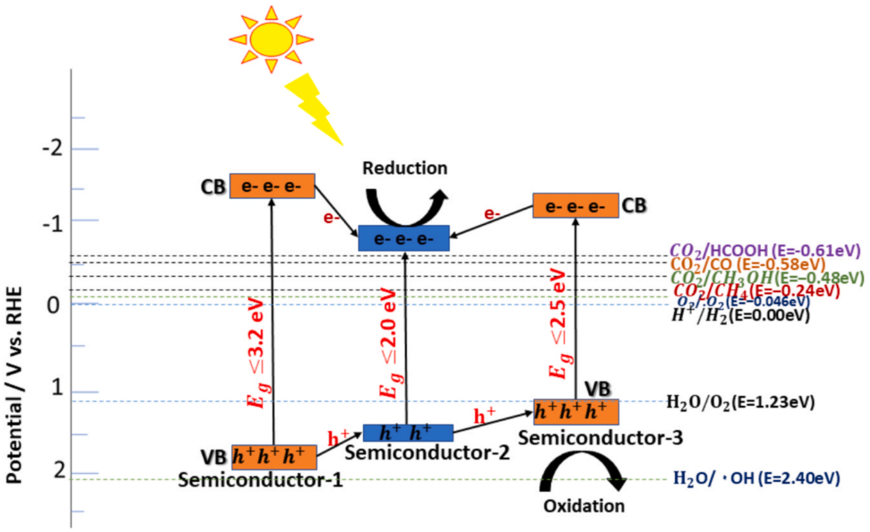

**Fig. 20.** Scheme for semiconductors with different band alignments for transportation of charge carriers.

chemically stable and react in the presence of oxygen and water. For industrial and environmental application metal oxides are preferred due to their better stability and recyclability for photocatalytic application.

## 5. Role of nano pyrophosphate in the catalyst for photocatalytic reactions

Nano pyrophosphates are basically nanoparticles composed of pyrophosphates having two phosphorus atoms and seven oxygen atoms. They play a significant role in catalysis due to their unique characteristics. i) They have high surface area and provide large number of active sites for catalytic reactions, ii) They have specific band gap energies which is comparable with the energy of solar light which generate electron-hole pairs, increase charge separation and reduce charge recombination, iii) The surface can be modified with various metals and metal oxides and improve the adsorption of reactants for better light absorption and charge transfer and iv) They are chemically and thermally stable and facilitate better photocatalytic reactions without degradation in the high temperature.

To get deep insight into the role of nano pyrophosphates different examples containing metal nano pyrophosphates would be discussed. Nickel pyrophosphate possesses good conductivity, large storage sites, broad channels for electrolyte ions movement, stable structure due to P-O bond. It is synthesized by co-precipitation method and used for degradation of methylene blue. 300-C calcined Nickel pyrophosphate nanoparticles were used for decolorization and degradation of 10ppm MB dye in the presence of UV and solar light. In the UV light source and 90 minutes stirring the mineralization efficiency reaches 83.1 %. Meanwhile, in the solar light MB dye solution exhibited 95.06 % photodegradation [156]. The photocatalytic mechanism of Nickel pyrophosphate nanoparticles is shown in Fig. 21. Similarly, Defect rich cobalt pyrophosphate modified with $Cd_{0.5}Zn_{0.5}S$ was synthesized for photocatalytic hydrogen generation. Cobalt-phosphonate-derived cobalt pyrophosphate hybrids (CoPPi-A) is a novel and hydrophilic cocatalyst with $Cd_{0.5}Zn_{0.5}S$ photocatalyst having controlled pH and optimized interface was used to produce 6.87mmolg$^{-1}$h$^{-1}$ photocatalytic hydrogen [157]. The nano pyrophosphates nanoparticles are advanced materials in the field of photocatalysis. They are widely used for water splitting and dye degradation from few days ago but their applications are very limited for $CO_2$ reduction and $H_2O_2$ production. The further development for the utilization of different kinds of nano pyrophosphates are required in the field of photocatalysis and energy

**Table 3**
Metal Sulfide-Metal Sulfide based composites for photocatalytic applications:.

| Photocatalysts-Sensitizers | Synthesis Methods | Heterojunctions | Activity | References |
|---|---|---|---|---|
| $MnIn_2S_4$-$Cu_7S_4$ | Oil bath stirring-Hydrothermal | Type-II | Photocatalytic production of $H_2$ is 13.81 μmol/g/h | [140] |
| CdS-$Bi_2S_3$ | Sono chemical-Sono chemical | Type-II | Photocatalytic production of $H_2$ is 5500 μmol/g/h | [141] |
| CdS-ZnS | AACVD-AACVD | Type-II | Photocurrent density is 8.02 mA/$cm^2$ vs. NHE | [142] |
| $In_2S_3$-$CdIn_2S_4$ | Cation exchange reaction-hydrothermal | Type-II | Photocatalytic production of CO is 825 μmol h$^{-1}$ g$^{-1}$ from $CO_2$ reduction | [144] |
| CdS-$ZnIn_2S_4$ | Water bath heating-Solvothermal | Direct Z-scheme | Photocatalytic production of $H_2$ is 540.3 μmol/g/h | [145] |
| $Bi_2S_3$-$SnIn_4S_8$ | Solvothermal-Solvothermal | Direct Z-scheme | Photodegradation of Rh B is 99.87 % | [146] |
| $MoSe_2$-$Bi_2S_3$-CdS | Solvothermal-Hydrothermal-Hydrothermal | Dual Direct Z-scheme | Photocatalytic production of $H_2$ is 11840 μmol/g/h | [147] |
| CdS-$MoS_2$ QDs-ZIS | Solvothermal-Solvothermal-Hydrothermal | Solid-state Z-scheme | $H_2$ production is 2107.5 μmol/g/h | [148] |
| ZnS-rGO-$Bi_2S_3$ | Hydrothermal-Hydrothermal-Hydrothermal | Solid-state Z-scheme | $H_2$ production is 2523.4 μmol/g/h and photocurrent density are 38 mA/$cm^2$ | [149] |
| Cd/CdS-$Co_9S_8$ | Hydrothermal-Sacrificial Template method | Solid-state Z-scheme | $H_2$ production is 10.42 μmol/h | [150] |
| CdS-$FeS_2$ | Hydrothermal-Hydrothermal | S-scheme | Photocatalytic production of $H_2$ is 107.56 μmol/g/h | [151] |
| ZIS-$FeS_2$ | Water-bath Hydrothermal | S-scheme | Photocatalytic production of $H_2$ is 10100 μmol/g/h | [152] |
| ZnS-ZIS | Hydrothermal-hydrothermal | S-scheme | $H_2$ production is 2912.3 μmol/g/h | [153] |
| CuS-ZIS | Hydrothermal-Hydrothermal | S-scheme | $H_2$ production is 4653.43 μmol/g/h | [154] |
| $Bi_2S_3$/CdS | Hydrothermal | S-scheme | $H_2O_2$ production 212.82 μmol L$^{-1}$ | [155] |

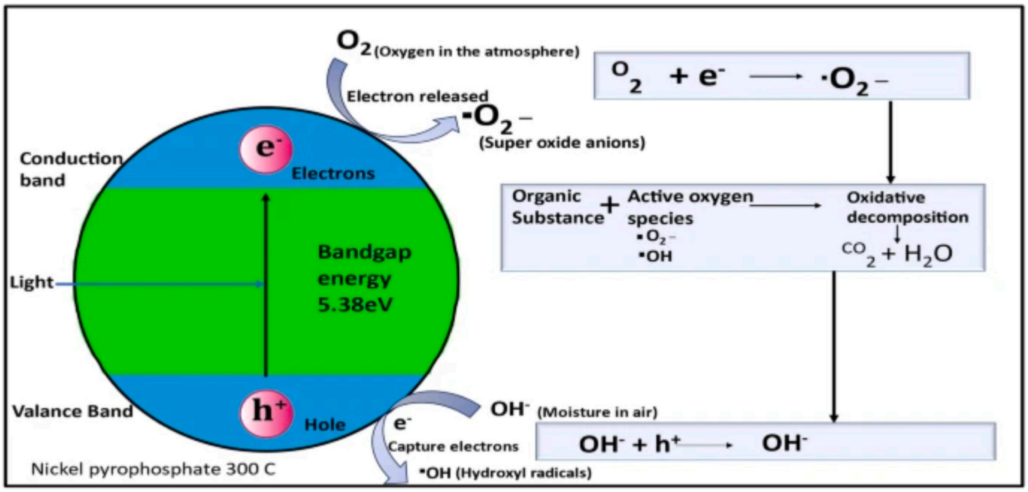

**Fig. 21.** Photocatalytic mechanism of Ni2P2O nanoparticles. Reproduced with permission [156]. Copyright 2024, Journal Material Sciences.

storage applications.

## 6. Conclusion and future perspectives

In the last few years, many investigations have been reported on constructing heterojunctions in binary and ternary composites of metal oxides and metal sulfides for photocatalysis. In this review article, the incisive appraisal on recent achievements in the area of heterojunction to improve water splitting, $CO_2$ reduction, photodegradation of dyes and $H_2O_2$ production by low-cost metal oxides and metal sulfides is presented. To create heterojunction between the photocatalysts systematic strategies are discussed. The strategies include band position alignment for charge transfer, formation of interface to produce internal electric field, charge separation and recombination of useless charge carriers and finally reduction of protons to produce hydrogen, reduction of $CO_2$ to produce alcohols, formic acid, CO and oxidation of dyes. It is further improved by surface modification like; by producing surface plasmon resonance effect and conductive bridges in between the photocatalysts. Further directions in this area should be focused on these aspects: i) More advancement in the morphology, interface formation and crystal structure to improve the stability of metal sulfides and to reduce the band gap of metal oxides are needed, ii) Utilization of noble metals and transition metal as SPR and conductive bridge for charge transfer and production of internal electric field in binary, ternary and quaternary heterojunctions should be studied further to improve the activities of photocatalysts commercially, iii) To design multicomponent photocatalysts proper understanding of interactions between layers, positive response to visible light, shortening of band gap and stability after heterojunction should be upgraded and iv) Cost effective and optimal metal oxide and metal sulfide cocatalysts and catalysts should be used as protective layer to make the environment pollution free.

After getting deeper insight into all type of heterojunctions there are few future development technology for formation of heterojunctions are needed: (i) Explore heterojunctions with ternary and quaternary semiconductors for optimization of band alignment, enhancing the light absorption spectrum and charge carrier dynamics (ii) Development of specific techniques to control heterojunction interface, improve charge carrier kinetics and long-term stability (iii) Advanced nanofabrication techniques are required to create heterojunctions with controlled dimension and high surface area to facilitate rapid charge transfer (iv) In situ and operando characterization methods are required to study the heterojunction dynamics with realistic operating conditions such as computational simulation and modeling for proper band alignment and charge transfer mechanisms (v) Foster collaboration between academia and industry is needed to harness the heterojunction potential for addressing global challenges and creating new opportunities in energy applications and environmental sustainability.

## CRediT authorship contribution statement

**Alisha Shabbir:** Writing – original draft, Formal analysis, Data curation, Investigation, Methodology. **Asad Mumtaz:** Writing – review & editing, Visualization, Validation, Supervision, Software, Resources, Project administration, Methodology, Investigation, Conceptualization, Writing – original draft. **Sabahat Sardar:** Writing – review & editing, Validation, Data curation, Writing – original draft.

## Declaration of Competing Interest

The authors declare that they have no known competing financial interests or personal relationships that could have appeared to influence the work reported in this paper.

## Data Availability

Data will be made available on request.

## Acknowledgement

We acknowledge the internal funding provided by the Department of Chemistry, School of Natural Sciences (SNS), National University of Sciences and Technology (NUST), Islamabad.

### *Interest statement*

Authors declare no competing financial interests.

## References

[1] R.A. El-Gendy, et al., Metal chalcogenides (CuS or MoS2)-modified TiO2 as highly efficient bifunctional photocatalyst nanocomposites for green H2 generation and dye degradation, Sci. Rep. 13 (1) (2023) 7994.
[2] E. Karamian, S. Sharifnia, On the general mechanism of photocatalytic reduction of CO2, J. CO2 Util. 16 (2016) 194–203.
[3] N. Shi, et al., Artificial chloroplast: Au/chloroplast-morph-TiO2 with fast electron transfer and enhanced photocatalytic activity, Int. J. Hydrog. Energy 39 (11) (2014) 5617–5624.
[4] I. Dincer, C. Acar, Review and evaluation of hydrogen production methods for better sustainability, Int. J. Hydrog. Energy 40 (34) (2015) 11094–11111.
[5] N. Chouhan, et al., Visible light harvesting Pt/CdS/Co-doped ZnO nanorods molecular device for hydrogen generation, Int. J. Hydrog. Energy 41 (4) (2016) 2298–2306.
[6] J. Wen, et al., A review on g-C3N4-based photocatalysts, Appl. Surf. Sci. 391 (2017) 72–123.

[7] G.L. Chiarello, M.H. Aguirre, E. Selli, Hydrogen production by photocatalytic steam reforming of methanol on noble metal-modified TiO2, J. Catal. 273 (2) (2010) 182–190.

[8] V. Etacheri, et al., Visible-light activation of TiO2 photocatalysts: Advances in theory and experiments, J. Photochem. Photobiol. C: Photochem. Rev. 25 (2015) 1–29.

[9] G. Colón, Towards the hydrogen production by photocatalysis, Appl. Catal. A: Gen. 518 (2016) 48–59.

[10] K. Maeda, Photocatalytic water splitting using semiconductor particles: history and recent developments, J. Photochem. Photobiol. C: Photochem. Rev. 12 (4) (2011) 237–268.

[11] C. Zamfirescu, G. Naterer, I. Dincer, Photo-electro-chemical chlorination of cuprous chloride with hydrochloric acid for hydrogen production, Int. J. Hydrog. Energy 37 (12) (2012) 9529–9536.

[12] C. Zamfirescu, I. Dincer, G. Naterer, Analysis of a photochemical water splitting reactor with supramolecular catalysts and a proton exchange membrane, Int. J. Hydrog. Energy 36 (17) (2011) 11273–11281.

[13] B. Liu, et al., Thermodynamic and kinetic analysis of heterogeneous photocatalysis for semiconductor systems, Phys. Chem. Chem. Phys. 16 (19) (2014) 8751–8760.

[14] N. Fajrina, M. Tahir, A critical review in strategies to improve photocatalytic water splitting towards hydrogen production, Int. J. Hydrog. Energy 44 (2) (2019) 540–577.

[15] M. Saeed, et al., Photocatalysis: An effective tool for photodegradation of dyes—A review, Environ. Sci. Pollut. Res. 29 (1) (2022) 293–311.

[16] M. Adeel, et al., Synthesis and characterization of Co–ZnO and evaluation of its photocatalytic activity for photodegradation of methyl orange, ACS Omega 6 (2) (2021) 1426–1435.

[17] Y.-H. Chiu, et al., Mechanistic insights into photodegradation of organic dyes using heterostructure photocatalysts, Catalysts 9 (5) (2019) 430.

[18] S. Fang, et al., Photocatalytic CO2 reduction, Nat. Rev. Methods Prim. 3 (1) (2023) 61.

[19] X. Xiang, F. Pan, Y. Li, A review on adsorption-enhanced photoreduction of carbon dioxide by nanocomposite materials, Adv. Compos. Hybrid. Mater. 1 (2018) 6–31.

[20] Mavrič, T., *Synthesis and characterization of metal/semiconductor nanocomposites for photocatalysis*. 2017, Univerza v Novi Gorici, Fakulteta za podiplomski študij.

[21] T. Inoue, et al., Photoelectrocatalytic reduction of carbon dioxide in aqueous suspensions of semiconductor powders, Nature 277 (5698) (1979) 637–638.

[22] U. Ulmer, et al., Fundamentals and applications of photocatalytic CO2 methanation, Nat. Commun. 10 (1) (2019) 3169.

[23] G. Yasin, et al., Defects-engineered tailoring of tri-doped interlinked metal-free bifunctional catalyst with lower gibbs free energy of OER/HER intermediates for overall water splitting, Mater. Today Chem. 23 (2022) 100634.

[24] R. Gandhi, A. Moses, S.S. Baral, Fundamental study of the photocatalytic reduction of CO2: A short review of thermodynamics, kinetics and mechanisms, Chem. Process Eng. 43 (2) (2022) 223–228.

[25] X. Xu, et al., The photocatalytic H2O2 production by metal-free photocatalysts under visible-light irradiation, Appl. Catal. B: Environ. (2023) 123271.

[26] Z. Chen, et al., Photocatalytic H2O2 production Systems: Design strategies and environmental applications, Chem. Eng. J. 451 (2023) 138489.

[27] J. Yang, et al., Engineering 2D photocatalysts for solar hydrogen peroxide production, Adv. Energy Mater. (2024) 2400740.

[28] S.H. Vosko, L. Wilk, M. Nusair, Accurate spin-dependent electron liquid correlation energies for local spin density calculations: a critical analysis, Can. J. Phys. 58 (8) (1980) 1200–1211.

[29] S. Hirata, M. Head-Gordon, Time-dependent density functional theory within the Tamm–Dancoff approximation, Chem. Phys. Lett. 314 (3-4) (1999) 291–299.

[30] P. Guiglion, C. Butchosa, M.A. Zwijnenburg, Polymeric watersplitting photocatalysts; a computational perspective on the water oxidation conundrum, J. Mater. Chem. A 2 (30) (2014) 11996–12004.

[31] C. Butchosa, P. Guiglion, M.A. Zwijnenburg, Carbon nitride photocatalysts for water splitting: a computational perspective, J. Phys. Chem. C. 118 (43) (2014) 24833–24842.

[32] L. Lin, et al., Treatment of produced water with photocatalysis: Recent advances, affecting factors and future research prospects, Catalysts 10 (8) (2020) 924.

[33] D. Zheng, et al., Nanocatalysts in photocatalytic water splitting for green hydrogen generation: Challenges and opportunities, J. Clean. Prod. (2023) 137700.

[34] K. Vinodgopal, P.V. Kamat, Enhanced rates of photocatalytic degradation of an azo dye using SnO2/TiO2 coupled semiconductor thin films, Environ. Sci. Technol. 29 (3) (1995) 841–845.

[35] K.T. Ranjit, B. Viswanathan, Synthesis, characterization and photocatalytic properties of iron-doped TiO2 catalysts, J. Photochem. Photobiol. A: Chem. 108 (1) (1997) 79–84.

[36] H. Zhou, et al., Towards highly efficient photocatalysts using semiconductor nanoarchitectures, Energy Environ. Sci. 5 (5) (2012) 6732–6743.

[37] L. Guo, et al., Morphology engineering of type-II heterojunction nanoarrays for improved sonophotocatalytic capability, Ultrason. Sonochem. 81 (2021) 105849.

[38] X. Meng, et al., Boosting hydrogen evolution performance of a CdS-based photocatalyst: in situ transition from type I to type II heterojunction during photocatalysis, ACS Catal. 12 (16) (2022) 10115–10126.

[39] J. Low, et al., Heterojunction photocatalysts, Adv. Mater. 29 (20) (2017) 1601694.

[40] P. Zhou, J. Yu, M. Jaroniec, All-solid-state Z-scheme photocatalytic systems, Adv. Mater. 26 (29) (2014) 4920–4935.

[41] J. Low, et al., A review of direct Z-scheme photocatalysts, Small Methods 1 (5) (2017) 1700080.

[42] P. Raizada, et al., An overview of converting reductive photocatalyst into all solid-state and direct Z-scheme system for water splitting and CO2 reduction, J. Ind. Eng. Chem. 93 (2021) 1–27.

[43] X. Li, et al., Two-dimensional sulfur-and chlorine-codoped g-C3N4/CdSe-amine heterostructures nanocomposite with effective interfacial charge transfer and mechanism insight, Appl. Catal. B: Environ. 280 (2021) 119452.

[44] Z. Wang, et al., S-scheme porous g-C3N4/Ag2MoO4 heterojunction composite for CO2 photoreduction, Chin. J. Struct. Chem. 41 (6) (2022) 2206015–2206022.

[45] T. Yang, et al., Ipolymer Cd3 (C3N3S3) 2/Zn3 (C3N3S3) 2 S-scheme heterojunction enhances photocatalytic H2 production, Chin. J. Catal. 58 (2024) 157–167.

[46] L. Wang, et al., S-scheme heterojunction photocatalysts for CO2 reduction, Matter 5 (12) (2022) 4187–4211.

[47] F. Li, et al., A review of updated S-scheme heterojunction photocatalysts, J. Mater. Sci. Technol. (2023).

[48] Q. Xu, et al., S-scheme heterojunction photocatalyst, Chem 6 (7) (2020) 1543–1559.

[49] A. Balapure, J.R. Dutta, R. Ganesan, Recent advances in semiconductor heterojunction: a detailed review of fundamentals of the photocatalysis, charge transfer mechanism, and materials, RSC Appl. Interfaces (2023).

[50] V. Hasija, et al., Step-scheme heterojunction photocatalysts for solar energy, water splitting, CO 2 conversion, and bacterial inactivation: a review, Environ. Chem. Lett. 19 (2021) 2941–2966.

[51] C. Cheng, et al., An inorganic/organic S-scheme heterojunction H2-production photocatalyst and its charge transfer mechanism, Adv. Mater. 33 (22) (2021) 2100317.

[52] X. Fei, et al., DFT study on regulating the electronic structure and CO2 reduction reaction in BiOBr/Sulphur-Doped G-C3N4 S-scheme heterojunctions, Front. Nanotechnol. 3 (2021) 698351.

[53] C. Li, et al., Construction of Z-scheme InN/BTe heterostructure for enhanced photocatalytic hydrogen evolution: DFT calculation and mechanism study, Int. J. Hydrog. Energy 68 (2024) 289–296.

[54] Y. Yang, et al., TiO 2/In 2 S 3 S-scheme photocatalyst with enhanced H 2 O 2-production activity, Nano Res. (2021) 1–9.

[55] C.V. Reddy, et al., Hetero-nanostructured metal oxide-based hybrid photocatalysts for enhanced photoelectrochemical water splitting–a review, Int. J. Hydrog. Energy 45 (36) (2020) 18331–18347.

[56] X. Li, et al., Recent progress in metal oxide-based photocatalysts for CO2 reduction to solar fuels: a review, Molecules 28 (4) (2023) 1653.

[57] V. Gadore, S.R. Mishra, M. Ahmaruzzaman, Metal sulphides and their heterojunctions for photocatalytic degradation of organic dyes-A comprehensive review, Environ. Sci. Pollut. Res. 30 (39) (2023) 90410–90457.

[58] G.G. Bessegato, et al., Achievements and trends in photoelectrocatalysis: from environmental to energy applications, Electrocatalysis 6 (2015) 415–441.

[59] S. McMichael, P. Fernández-Ibáñez, J.A. Byrne, A review of photoelectrocatalytic reactors for water and wastewater treatment, Water 13 (9) (2021) 1198.

[60] L. Flannery, et al., WWMOD? What would metal oxides do?: Redefining their applicability in today’s energy technologies, Polyhedron 170 (2019) 334–358.

[61] Y. Yang, et al., Progress in developing metal oxide nanomaterials for photoelectrochemical water splitting, Adv. Energy Mater. 7 (19) (2017) 1700555.

[62] X. Jia, et al., Transforming type-I to type-II heterostructure photocatalyst via energy band engineering: a case study of I-BiOCl/I-BiOBr, Appl. Catal. B: Environ. 204 (2017) 505–514.

[63] H. Cai, et al., Orienting the charge transfer path of type-II heterojunction for photocatalytic hydrogen evolution, Appl. Catal. B: Environ. 256 (2019) 117853.

[64] X. Chai, et al., 3D ordered urchin-like TiO2@ Fe2O3 arrays photoanode for efficient photoelectrochemical water splitting, Appl. Surf. Sci. 470 (2019) 668–676.

[65] K. Zhang, et al., Architecture lattice-matched cauliflower-like CuO/ZnO p–n heterojunction toward efficient water splitting, J. Chem. Technol. Biotechnol. 97 (4) (2022) 914–923.

[66] Y. Pihosh, et al., Nanostructured WO3/BiVO4 photoanodes for efficient photoelectrochemical water splitting, Small 10 (18) (2014) 3692–3699.

[67] I. Castro, et al., Charge transfer mechanism of WO3/TiO2 heterostructure for photoelectrochemical water splitting, J. Photochem. Photobiol. A: Chem. 339 (2017) 95–102.

[68] C. Hao, et al., Enhanced photoelectrochemical water splitting with TiO2@ Ag2O nanowire arrays via pn heterojunction formation, Sol. Energy Mater. Sol. Cells 174 (2018) 132–139.

[69] L. Yao, et al., Chemical bath deposition synthesis of TiO2/Cu2O core/shell nanowire arrays with enhanced photoelectrochemical water splitting for H2 evolution and photostability, Int. J. Hydrog. Energy 43 (33) (2018) 15907–15917.

[70] W. Wang, et al., Heterostructured TiO2 nanorod@ nanobowl arrays for efficient photoelectrochemical water splitting, Small 12 (11) (2016) 1469–1478.

[71] S. Siuleiman, et al., Photodegradation of Orange II by ZnO and TiO2 powders and nanowire ZnO and ZnO/TiO2 thin films, Colloids Surf. A: Physicochem. Eng. Asp. 460 (2014) 408–413.

[72] F. Achouri, et al., Aqueous synthesis and enhanced photocatalytic activity of ZnO/Fe2O3 heterostructures, J. Phys. Chem. Solids 75 (10) (2014) 1081–1087.

[73] J. Wang, et al., Rapid toxicity elimination of organic pollutants by the photocatalysis of environment-friendly and magnetically recoverable step-scheme SnFe2O4/ZnFe2O4 nano-heterojunctions, Chem. Eng. J. 379 (2020) 122264.

[74] J. Zhang, et al., Environment-friendly ternary ZnO/ZnFe2O4/TiO2 composite photocatalyst with synergistic enhanced photocatalytic activity under visible-light irradiation, Solid State Sci. 129 (2022) 106913.

[75] F. Iqbal, et al., Photocatalytic reduction of CO2 to methanol over ZnFe2O4/TiO2 (p–n) heterojunctions under visible light irradiation, J. Chem. Technol. Biotechnol. 95 (8) (2020) 2208–2221.

[76] M. Abbas, et al., WO3-x nanorods/rGO/AgBiS2 Z-scheme heterojunction with comprehensive spectrum response and enhanced Fenton and photocatalytic activities, J. Colloid Interface Sci. 662 (2024) 250–262.

[77] M. Abbas, et al., Unlocking enhanced photo-Fenton, night-Fenton, and photocatalytic activities of dual Z-scheme MoS2/WO3–x/Ag2S core-shell structure via defect engineering, J. Mater. Sci. Technol. 197 (2024) 160–170.

[78] Y. Zhang, et al., GeC/SnSe2 van der waals heterostructure: A promising direct Z-scheme photocatalyst for overall water splitting with strong optical absorption, high solar-to-hydrogen energy conversion efficiency and superior catalytic activity, Int. J. Hydrog. Energy 70 (2024) 357–369.

[79] H. Derikvand, N. Tahmasebi, S. Barzegar, Construction of a direct Z-scheme Cs3Bi2Cl9/g-C3N4 heterojunction composite for efficient photocatalytic degradation of various pollutants in water: Performance, kinetics and degradation mechanism, Chemosphere 355 (2024) 141879.

[80] K.-X. Xie, et al., A direct Z-scheme GeS/GeSe van der Waals heterojunction as a promising photocatalyst with high optical absorption, solar-to-hydrogen efficiency and catalytic activity for overall water splitting: First-principles prediction, Int. J. Hydrog. Energy 51 (2024) 1381–1391.

[81] Q. Xu, et al., Direct Z-scheme photocatalysts: Principles, synthesis, and applications, Mater. Today 21 (10) (2018) 1042–1063.

[82] T. Zhou, et al., Bird-nest structured ZnO/TiO2 as a direct Z-scheme photoanode with enhanced light harvesting and carriers kinetics for highly efficient and stable photoelectrochemical water splitting, Appl. Catal. B: Environ. 267 (2020) 118599.

[83] P. Dhiman, et al., Robust magnetic ZnO-Fe2O3 Z-scheme hetereojunctions with in-built metal-redox for high performance photo-degradation of sulfamethoxazole and electrochemical dopamine detection, Environ. Res. 197 (2021) 111074.

[84] Y. Chen, et al., Polarization-Enhanced direct Z-scheme ZnO-WO3-x nanorod arrays for efficient piezoelectric-photoelectrochemical Water splitting, Appl. Catal. B: Environ. 259 (2019) 118079.

[85] S. Ghattavi, A. Nezamzadeh-Ejhieh, A double-Z-scheme ZnO/AgI/WO3 photocatalyst with high visible light activity: experimental design and mechanism pathway in the degradation of methylene blue, J. Mol. Liq. 322 (2021) 114563.

[86] Z. Xie, et al., Construction of CuO quantum Dots/WO3 nanosheets 0D/2D Z-scheme heterojunction with enhanced photocatalytic CO2 reduction activity under visible-light, J. Alloy. Compd. 858 (2021) 157668.

[87] M.E. Aguirre, et al., Cu2O/TiO2 heterostructures for CO2 reduction through a direct Z-scheme: Protecting Cu2O from photocorrosion, Appl. Catal. B: Environ. 217 (2017) 485–493.

[88] H. Yu, et al., All-solid-state Z-scheme nanojunction PW12/Ag/ZnO photocatalyst: Effective carriers transfer promotion and enhanced visible light driven, J. Mol. Struct. 1300 (2024) 137272.

[89] F. Chen, et al., Recent Progress in All-Solid-State Z-scheme Heterostructures for Photoreduction of CO2, ChemCatChem (2024) e202301492.

[90] M. Tahir, Well-designed ZnFe2O4/Ag/TiO2 nanorods heterojunction with Ag as electron mediator for photocatalytic CO2 reduction to fuels under UV/visible light, J. CO2 Util. 37 (2020) 134–146.

[91] Y. Fu, et al., A ternary nanostructured α-Fe2O3/Au/TiO2 photoanode with reconstructed interfaces for efficient photoelectrocatalytic water splitting, Appl. Catal. B: Environ. 260 (2020) 118206.

[92] B. Chen, et al., Rational design of all-solid-state TiO2-x/Cu/ZnO Z-scheme heterojunction via ALD-assistance for enhanced photocatalytic activity, J. Colloid Interface Sci. 607 (2022) 760–768.

[93] H. Li, et al., Z-scheme Ag2O/Ag/amorphous TiO2 shells for enhanced plasmonic photoelectrochemical assay of nitrogen dioxide, Sens. Actuators B: Chem. 289 (2019) 138–143.

[94] Q. Sun, et al., The enhanced photocatalytic activity of Ag-Fe2O3-TiO2 performed in Z-scheme route associated with localized surface plasmon resonance effect, Colloids Surf. A: Physicochem. Eng. Asp. 628 (2021) 127304.

[95] N.H. Shah, et al., Redeeming the photocatalytic potential of CuWO4 incorporating Ag6Si2O7 via S-scheme PN heterostructure, J. Alloy. Compd. 983 (2024) 173895.

[96] J. Hua, et al., A hierarchical Bi-MOF-derived BiOBr/Mn0. 2Cd0. 8S S-scheme for visible-light-driven photocatalytic CO2 reduction, J. Mater. Sci. Technol. 156 (2023) 64–71.

[97] Z. Zhao, et al., Interfacial chemical bond and oxygen vacancy-enhanced In2O3/CdSe-DETA S-scheme heterojunction for photocatalytic CO2 conversion, Adv. Funct. Mater. 33 (23) (2023) 2214470.

[98] B. Zhu, et al., Construction of 2D S-scheme heterojunction photocatalyst, Adv. Mater. 36 (8) (2024) 2310600.

[99] T. Li, N. Tsubaki, Z. Jin, S-scheme heterojunction in photocatalytic hydrogen production, J. Mater. Sci. Technol. 169 (2024) 82–104.

[100] P. Hao, et al., Recent advances, application and prospect in g-C3N4-based S-scheme heterojunction photocatalysts, Sep. Purif. Technol. 330 (2024) 125302.

[101] J. Gao, et al., Dimensional-matched two dimensional/two dimensional TiO2/Bi2O3 step-scheme heterojunction for boosted photocatalytic performance of sterilization and water splitting, J. Colloid Interface Sci. 628 (2022) 166–178.

[102] H. Deng, et al., S-scheme heterojunction based on p-type ZnMn2O4 and n-type ZnO with improved photocatalytic CO2 reduction activity, Chem. Eng. J. 409 (2021) 127377.

[103] Z. Jiang, et al., S-scheme ZnO/WO3 heterojunction photocatalyst for efficient H2O2 production, J. Mater. Sci. Technol. 124 (2022) 193–201.

[104] S. Zamani, et al., WO3/Ag/ZnO S-scheme heterostructure thin film spinning disc photoreactor for intensified photodegradation of cephalexin antibiotic, Chemosphere 307 (2022) 135812.

[105] F. Mukhtar, et al., Dual S-scheme heterojunction ZnO–V2O5–WO3 nanocomposite with enhanced photocatalytic and antimicrobial activity, Mater. Chem. Phys. 263 (2021) 124372.

[106] G. Zhang, et al., Preparation of Ga2O3/ZnO/WO3 double S-scheme heterojunction composite nanofibers by electrospinning method for enhancing photocatalytic activity, J. Mater. Sci.: Mater. Electron. 32 (6) (2021) 7307–7318.

[107] B. He, et al., Cooperative coupling of H2O2 production and organic synthesis over a floatable polystyrene-sphere-supported TiO2/Bi2O3 S-Scheme photocatalyst, Adv. Mater. 34 (38) (2022) 2203225.

[108] M.M. Khan, S.F. Adil, A. Al-Mayouf, Metal oxides as photocatalysts, Elsevier (2015) 462–464.

[109] J. Grosskreutz, Mechanical properties of metal oxide films, J. Electrochem. Soc. 116 (9) (1969) 1232.

[110] M.B. Tahir, et al., Metal oxide-and metal sulfide-based nanomaterials as photocatalysts. in *Nanotechnology and Photocatalysis for Environmental Applications*, Elsevier, 2020, pp. 77–96.

[111] D. Kong, et al., AgFeO2 nanoparticle/ZnIn2S4 microsphere p–n heterojunctions with hierarchical nanostructures for efficient visible-light-driven H2 evolution, ACS Sustain. Chem. Eng. 9 (7) (2021) 2673–2683.

[112] L.K. Dhandole, et al., CdIn2S4 chalcogenide/TiO2 nanorod heterostructured photoanode: an advanced material for photoelectrochemical applications 490 (2019) 18–29.

[113] Q. Liu, et al., 2D ZnIn2S4 nanosheet/1D TiO2 nanorod heterostructure arrays for improved photoelectrochemical water splitting 6 (19) (2014) 17200–17207.

[114] A. Ahmad, et al., Three dimensional rosette-rod TiO2/Bi2S3 heterojunction for enhanced photoelectrochemical water splitting 868 (2021) 159133.

[115] R.R. Prabhakar, et al., Sb2S3/TiO2 heterojunction photocathodes: band alignment and water splitting properties 32 (17) (2020) 7247–7253.

[116] X. Wang, et al., Wedged ß-In2S3 sensitized TiO2 films for enhanced photoelectrochemical hydrogen generation 831 (2020) 154798.

[117] F. Tezcan, et al., Criss-crossed α-Fe2O3 nanorods/Bi2S3 heterojunction for enhanced photoelectrochemical water splitting, Fuel 324 (2022) 124477.

[118] W. Dang, et al., Fabrication of multilayer 1D TiO2/CdS/ZnS with high photoelectrochemical performance and enhanced stability, J. Alloy. Compd. 886 (2021) 161329.

[119] T. Bhat, et al., TiO2/PbS/ZnS heterostructure for panchromatic quantum dot sensitized solar cells synthesized by wet chemical route, Opt. Mater. 73 (2017) 781–792.

[120] M. Han, et al., Combined heterostructures between Bi2S3 nanosheets and H2-treated TiO2 nanorods for enhanced photoelectrochemical water splitting 598 (2022) 153850.

[121] A. Meng, et al., Direct Z-scheme TiO2/CdS hierarchical photocatalyst for enhanced photocatalytic H2-production activity 422 (2017) 518–527.

[122] Q. Luan, et al., Construction of 2D-ZnS@ ZnO Z-Scheme Heterostructured Nanosheets with a Highly Ordered ZnO Core and Disordered ZnS Shell for Enhancing Photocatalytic Hydrogen Evolution, ChemNanoMat 6 (3) (2020) 470–479.

[123] J. Murillo-Sierra, et al., Construction of direct Z-scheme WO3/ZnS heterojunction to enhance the photocatalytic degradation of tetracycline antibiotic, J. Environ. Chem. Eng. 9 (2) (2021) 105111.

[124] F. Xu, et al., Direct Z-scheme TiO2/NiS core–shell hybrid nanofibers with enhanced photocatalytic H2-production activity, ACS Sustain. Chem. Eng. 6 (9) (2018) 12291–12298.

[125] Z.-H. Wei, et al., Enhanced photocatalytic CO2 reduction activity of Z-scheme CdS/BiVO4 nanocomposite with thinner BiVO4 nanosheets, J. CO2 Util. 28 (2018) 15–25.

[126] X. Xu, et al., Construction of Z-scheme CdS/Ag/TiO2 NTs photocatalysts for photocatalytic dye degradation and hydrogen evolution, Spectrochim. Acta Part A: Mol. Biomol. Spectrosc. 276 (2022) 121215.

[127] Q. Ma, et al., Strategic modulation of electron migration in the TiO2-Au-CdS: Z-scheme design for the enhancement in hydrogen evolution reaction, Electrochem. Commun. 95 (2018) 28–32.

[128] H. Zhao, et al., Synergistic promotion of solar-driven H2 generation by three-dimensionally ordered macroporous structured TiO2-Au-CdS ternary photocatalyst, Appl. Catal. B: Environ. 184 (2016) 182–190.

[129] N. Zhang, et al., Vertically aligned ZnO–Au@ CdS core–shell nanorod arrays as an all-solid-state vectorial Z-scheme system for photocatalytic application, J. Mater. Chem. A 4 (48) (2016) 18804–18814.

[130] S. Liang, et al., 3D spatially branched hierarchical Z-scheme CdS-Au nanoclusters-ZnO hybrids with boosted photocatalytic hydrogen evolution, J. Alloy. Compd. 754 (2018) 105–113.

[131] H. Park, et al., CoS@ TiO2 S-scheme heterojunction photocatalyst for hydrogen production from photoinduced water splitting, J. Clean. Prod. 319 (2021) 128819.

[132] N. Güy, K. Atacan, M. Özacar, Rational construction of pnp CuO/CdS/CoWO4 S-scheme heterojunction with influential separation and directional transfer of interfacial photocarriers for boosted photocatalytic H2 evolution, Renew. Energy 195 (2022) 107–120.

[133] S. Chen, et al., Coupling the bioanode and S-scheme CuO/CdS quantum dots photocathode for chlortetracycline degradation: Performance, mechanism and microbial community, Process Saf. Environ. Prot. 166 (2022) 328–340.

[134] H. Ge, et al., S-scheme heterojunction TiO2/CdS nanocomposite nanofiber as H2-production photocatalyst, ChemCatChem 11 (24) (2019) 6301–6309.

[135] Z. Wang, et al., Step-scheme CdS/TiO2 nanocomposite hollow microsphere with enhanced photocatalytic CO2 reduction activity, J. Mater. Sci. Technol. 56 (2020) 143–150.

[136] A. Tikoo, et al., Mechanistic insights into enhanced photocatalytic H 2 O 2 production induced by a Z-scheme heterojunction of copper bismuth oxide and molybdenum sulfide, J. Mater. Chem. A 11 (27) (2023) 14887–14899.

[137] T. Hu, et al., Noble-metal-free Ni2P modified step-scheme SnNb2O6/CdS-diethylenetriamine for photocatalytic hydrogen production under broadband light irradiation, Appl. Catal. B: Environ. 269 (2020) 118844.

[138] Y. Liu, et al., Metal sulfide/MOF-based composites as visible-light-driven photocatalysts for enhanced hydrogen production from water splitting, Coord. Chem. Rev. 409 (2020) 213220.

[139] Q. Zhu, et al., Recent progress of metal sulfide photocatalysts for solar energy conversion, Adv. Mater. 34 (45) (2022) 2202929.

[140] Y. Song, et al., Cu7S4/MnIn2S4 heterojunction for efficient photocatalytic hydrogen generation, J. Alloy. Compd. 884 (2021) 161035.

[141] L.-X. Hao, et al., Sonochemistry synthesis of Bi2S3/CdS heterostructure with enhanced performance for photocatalytic hydrogen evolution, Int. J. Hydrog. Energy 39 (26) (2014) 14479–14486.

[142] J. Zhang, et al., High-performance CdS–ZnS core–shell nanorod array photoelectrode for photoelectrochemical hydrogen generation, J. Mater. Chem. A 3 (2) (2015) 535–541.

[143] J. Kundu, B.K. Satpathy, D. Pradhan, Composition-controlled CdS/ZnS heterostructure nanocomposites for efficient visible light photocatalytic hydrogen generation, Ind. Eng. Chem. Res. 58 (51) (2019) 22709–22717.

[144] S. Wang, et al., Formation of hierarchical In2S3–CdIn2S4 heterostructured nanotubes for efficient and stable visible light CO2 reduction, J. Am. Chem. Soc. 139 (48) (2017) 17305–17308.

[145] E. Zhang, et al., Visually resolving the direct Z-scheme heterojunction in CdS@ ZnIn2S4 hollow cubes for photocatalytic evolution of H2 and H2O2 from pure water, Appl. Catal. B: Environ. 293 (2021) 120213.

[146] H. Shi, et al., Construction of novel Z-scheme flower-like Bi2S3/SnIn4S8 heterojunctions with enhanced visible light photodegradation and bactericidal activity, Appl. Surf. Sci. 465 (2019) 212–222.

[147] K. Wang, et al., Hollow MoSe2@ Bi2S3/CdS core-shell nanostructure as dual Z-scheme heterojunctions with enhanced full spectrum photocatalytic-photothermal performance, Appl. Catal. B: Environ. 281 (2021) 119482.

[148] W. Chen, et al., Highly efficient visible-light-driven photocatalytic hydrogen evolution by all-solid-state Z-scheme CdS/QDs/ZnIn2S4 architectures with MoS2 quantum dots as solid-state electron mediator, Appl. Surf. Sci. 504 (2020) 144406.

[149] H. Park, et al., Switching of a type I to an all-solid-state Z-scheme heterojunction by an electron mediator rGO bridge: 18.4% solar-to-hydrogen efficiency in n-ZnS/rGO/p-Bi2S3 ternary catalyst, Chem. Eng. J. 430 (2022) 133104.

[150] T. Zhang, et al., Z-scheme transition metal bridge of Co9S8/Cd/CdS tubular heterostructure for enhanced photocatalytic hydrogen evolution, Appl. Catal. B: Environ. 286 (2021) 119853.

[151] M.S. Goh, et al., Sustainable and stable hydrogen production over petal-shaped CdS/FeS2 S-scheme heterojunction by photocatalytic water splitting, Int. J. Hydrog. Energy 47 (65) (2022) 27911–27929.

[152] K. Chen, et al., Construction of core–shell FeS2@ ZnIn2S4 hollow hierarchical structure S-scheme heterojunction for boosted photothermal-assisted photocatalytic H2 production, Chem. Eng. J. 454 (2023) 140053.

[153] J. Liu, et al., Interfacial intimacy and internal electric field modulated S-scheme Sv-ZnS/ZnIn2S4 photocatalyst for efficient H2 evolution and CO2 reduction, J. Colloid Interface Sci. 635 (2023) 284–294.

[154] Y. Wang, et al., Hollow Nanoboxes Cu2-xS@ ZnIn2S4 Core-Shell S-Scheme Heterojunction with Broad-Spectrum Response and Enhanced Photothermal-Photocatalytic Performance, Small 18 (31) (2022) 2202544.

[155] S.M. Ghoreishian, et al., Full-spectrum-responsive Bi2S3@ CdS S-scheme heterostructure with intimated ultrathin RGO toward photocatalytic Cr (VI) reduction and H2O2 production: Experimental and DFT studies, Chem. Eng. J. 419 (2021) 129530.

[156] P. Solanki, et al., Photocatalytic applications of Nickel pyrophosphate nano-particles in wastewater treatment, J. Mater. Sci.: Mater. Electron. 35 (17) (2024) 1141.

[157] L.-J. Gao, et al., Defect-rich cobalt pyrophosphate hybrids decorated Cd0. 5Zn0. 5S for efficient photocatalytic hydrogen evolution: Defect and interface engineering, J. Colloid Interface Sci. 606 (2022) 544–555.